Solar Irradiance Forecast from All-Sky images using Machine Learning

Von der Fakultät für Mathematik und Physik

der Gottfried Wilhelm Leibniz Universität Hannover

zur Erlangung des Grades

Doktor der Naturwissenschaften

- Dr. rer. nat. -

genehmigte Dissertation

von

M. Sc. Cristian Daniel Crisosto González

geboren am 15.11.1985 in Chillán, Chile

2023

Abstract

The novel method presented here comprises techniques for cloud coverage percentage forecasts, cloud movement forecast and the subsequently prediction of the global horizontal irradiance (GHI) using all-sky images and Machine Learning techniques. Such models are employed to forecast GHI, which is necessary to make more accurate time series forecasts for photovoltaic systems like "island solutions" for power production or for energy exchange like in virtual power plants. All images were recorded by a hemispheric sky imager (HSI) at the Institute of Meteorology and Climatology (IMuK) of the Leibniz University Hannover, Hannover, Germany.

This thesis is composed of three parts. First, a model to forecast the total cloud cover five-minutes ahead by training an autoregressive neural network with Backpropagation. The prediction results showed a reduction of both the Root Mean Square Error ($RMSE$) and Mean Absolute Error (MAE) by approximately 30% compared to the reference solar persistence solar model for various cloud conditions. Second, a model to predict the GHI up to one-hour ahead by training a Levenberg Marquardt Backpropagation neural network. This novel method reduced both the $RMSE$ and the MAE of the one-hour prediction by approximately 40% under various weather conditions. Third, for the forecasting of the cloud movement up to two-minutes ahead, a high-resolution Deep Learning method using convolutional neural networks (CNN) was created. By taking real cloud shapes produced by the correction of the hazy areas considering the green signal counts pixels, predicted clouds shapes of the proposed algorithm was compared with the persistence solar model using the Sørensen-Dice similarity coefficient (SDC). The results of the proposed method have shown a mean SDC of $94 \pm 2.6\%$ (mean $\pm$ standard deviation) for the first minutes outperforming the persistence solar model with a SDC of $89 \pm 3.8\%$. Thus, the proposed method may represent cloud shapes better than the persistence solar model. Finally, the Bonferroni's correction was performed so that the significance level of 0.05 was corrected to 0.05, and thus, the difference between the SDC of the proposed method and the persistence solar model was $p = 0.001$ being significantly high.

The proposed methodologies may have broad application in the planning and management of PV power production allowing more accurate forecasts of the GHI minutes ahead by targeting primary and secondary energy control reserve.

Keywords: Solar Irradiance, Machine Learning, Convolutional Neural Networks

Contents

List of Figures

1 Introduction

1.1 Motivation

The production of solar energy is subject to strong spatial and temporal fluctuations due to the dependence on meteorological boundary conditions. This leads to uncertainties in the planning of energy supplies and thus, to economic inefficiencies [1] - [2] . With a reliable solar performance forecast, uncertainty is minimized while load and storage management can be optimized [3] - [4]. Prediction of solar irradiation makes an important contribution to efficient and economical applications for many areas of solar energy use, while high-quality data series are the key to understanding the dynamic interaction of photovoltaic (PV) systems, loads, and grids [5].

The International Energy Agency (IEA) estimates that after 2060, solar energy could cover up to one third of the world's energy consumption. Therefore, the solar energy use is likely to grow by a double-digit rate throughout the world and for the next decades [6] - [7] . This trend makes photovoltaics an even more important alternative for global power supply. New models for the forecast of solar energy production could help to reduce the difficulties of integrating PV systems into existing power supply structures. In order to optimally manage the power supply, electricity producers are compelled to provide a forecast of the expected delivered quantities [6]. Most of the different concepts used to address the integration of renewable energy agree on the need for accurate predictions for the possible production and subsequent energy load to the electrical system [8]. Therefore, solar power forecasts will be an important contributor to the future power supply technologies, influencing the planning, profitability, and operation of power systems.

This thesis focuses on predicting global solar irradiance (GHI) up to one hour ahead in one-minute resolution. In order to support more accurate solar irradiance forecasts, three complementary methods utilizing machine learning models were investigated. The robustness and performance of generating those forecasts are estimated and evaluated.

1.2 Dataset

The goal of this work is to develop an algorithm to accurately forecast GHI. Thus, knowing the future position of the clouds as precisely as possible is fundamental. The focus of this section is to describe the datasets developed in this thesis.

1.2.1 Image acquisition

The pictures used for this study were recorded with both a Canon G10 and a Canon EOS 700D, using an exposure time of $1000/s$ and an acquisition time of 1-minute intervals. The Hemispherical Sky Imager (HSI), installed on the roof of IMuK, is a set of digital commercial compact CCD (charge-coupled device) cameras equipped with a fish-eye lens providing a 183° field of view. This provides hemispherical images of the entire sky. The maximum image size is $4416x3312$ pixels, corresponding to 3.5 million pixels for the hemispherical image with a radius of 1060 pixels. In addition, the results of Toshing et al., 2013 [9] demonstrated the development of a camera system at IMuK, where the projection of the camera system was found to be nearly equidistant.

1.2.2 Cloud pixel identification

The method developed and used at IMuK in order to extract the cloud cover fraction (CCF) from the RGB channels use an algorithm called *Sky-Index* (equation 1.1) based on the approach by Yamashita et al. [10] . The *Sky-Index* separates blue sky and cloud areas. Also, in order to improve cloud detection in the uncertainty range for *Sky-Index* of 0.14 and 0.2, another filter was implemented as detailed by Schrempf et al. [61] expanding 1.1 for a better cloud identification. This allows analysis of uncertain or hazy areas in the digital image by taking into account the green signal counts. This correction, called *Haze-Index* (equation 1.2), defines a hazy area if the value of the green signal count is greater than the average of red and blue. A cloud is defined by the haze filter if the green signal count is smaller than the average. The position of the sun in the image is also calculated in order to evaluate the brightest circular solar area with an additional sun filter. In contrast to the *Sky-Index*, the sun filter uses different thresholds, which can be optimized for the higher and saturated signal. Figure 1.1 shows an example using pictures from the HSI system installed in Hannover.

$$Sky - Index = \frac{count_{blue} - count_{red}}{count_{blue} + count_{red}}. \tag{1.1}$$

$$Haze - Index = \frac{\frac{count_{red} + count_{blue}}{2} + count_{green}}{\frac{count_{red} - count_{blue}}{2} - count_{green}}. \tag{1.2}$$

(a)   (b)   (c)
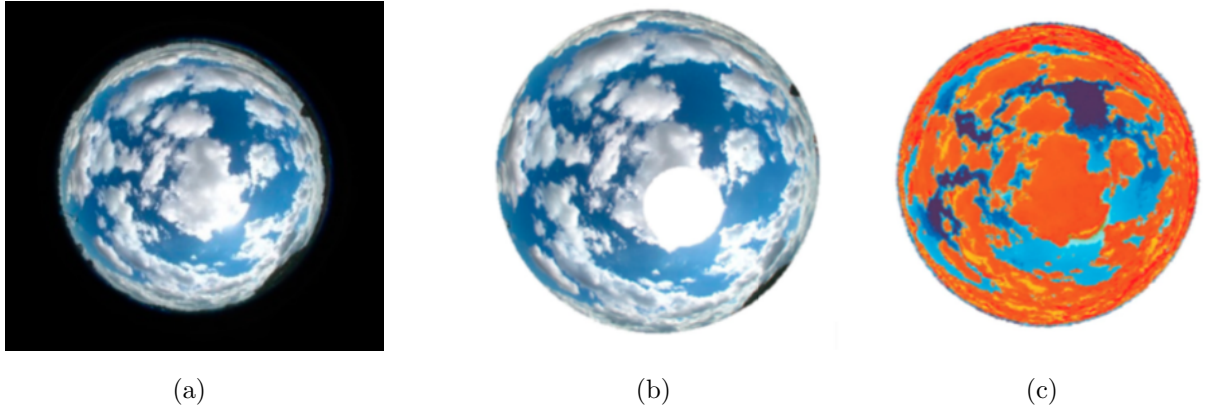
Figure 1.1: Image processing to extract the cloud cover fraction from the red-green-blue chan-
nels: (a) Original image from the all-sky image installed at IMuK in Hannover.
(b) Zoomed and cropped black area of the original image. The sun is covered for
a white circle. (c) *Haze-Index* image. Here we can see in predominantly orange
color the position of the cloud.

1.2.3 Global Horizontal Irradiance

Global Horizontal Irradiance (GHI) is the total amount of shortwave radiation received by
a horizontal surface on the ground [11]. The values obtained from the GHI are particularly
interesting for PV installations and are composed by the sum of the direct beam of the sun;
defined as Direct Normal Irradiance (DNI) and the indirect beam of the sun; defined as Diffuse
Horizontal Irradiance (DHI). The GHI was measured at IMuK with a Pyranometer CMP-11
by KippZonen [12]. A mathematical description of the GHI is given by:

$$GHI = DHI + DNI * \cos(Z)$$

where Z is the Solar Zenith Angle (SZA). In the formula, the ground reflected irradiation was
not taken into consideration because it can usually be insignificant compared with the DHI
and the DNI.

1.2.4 Sun Zenith Angle

The sun zenith angle (SZA), is defined as:

$$SZA = arcos(\sin\phi \cdot \sin\delta + \cos\omega \cdot \cos\phi \cdot \cos\delta),$$

in which ϕ was the declination of the sun, δ the latitude (latitude is defined positive in the north hemisphere) and ω the hour angle, in the local solar time. The SZA is a function of the day of the year and is independent of the location and is defined as the angle between the zenith and the centre of the sun.

The SZA algorithm used in this investigation, a free Matlab code sample [13], was extended at IMuK according to the needs of this work. The output of this program was one-minute solar position values for the location of IMuK. The SZA was the most important input parameter to train the network, helping it to learn patterns in the training phase and deliver the output parameters in the simulation phase. In addition, the software estimates the local time based on coordinated universal time UTC and longitude values.

1.3 Contents of the articles

The novel forecasting models are presented as a support for predicting cloud positions, and thus, global horizontal irradiance up to one-hour ahead using machine learning techniques. Additionally, tests and comparisons of the final algorithms with other benchmarks methods is conducted. In this thesis the terminology cloud coverage and cloud concentration will be used as synonym. The terminology cloud motion and cloud movement as well.

This work is composed of three published scientific articles. The articles will be explained in the following order:

Article A: *"Autoregressive Neural Network for Cloud Concentration Forecast from Hemispheric Sky Images"*. To accurately know the direction in which the clouds are moving in the next few minutes plays a fundamental role. Therefore, an autoregressive artificial neural network focused on clouds concentration forecast few minutes ahead was developed.

Article B: *"One-Hour Prediction of the Global Solar Irradiance from All-Sky Images Using Artificial Neural Networks"*. This article answers the question, how much energy will reach the surface at the Institute of Meteorology and Climatology (IMuK) one-hour ahead?.

Article C: *"Convolutional Neural Network for High-Resolution Cloud Motion Prediction from Hemispheric Sky Images"*. This article presents a convolutional neural network (CNN) to accurately predict cloud shapes up to two minutes ahead in high-resolution hemispherical sky images (HSI).

The following part of this thesis is structured as follows: Chapter 2 will be described the current literature utilized for this thesis. The methods and theory of artificial neural networks (ANN) and convolutional neural networks (CNN) are quickly described in Chapter 3. The published papers are shown in Chapter 4. The conclusions and outlook will be given in the Chapter 5.

2 Literatur review

The purpose of this chapter is to provide a literature review of the current technologies that are being employed in the solar irradiance forecasting around the world. We will look at literature associated with four different techniques that can be used to do solar irradiance forecasting. Mainly, through visual cloud movements that has been followed for most of the human history, then using Red-Green-Blue (RGB) pixels and Artificial Intelligence (AI) based on Convolutional Neural Networks (CNN) and Artificial Neural Networks (ANN). We will look at different techniques that have been employed by different academics and scientific institutions. We will also look into different practical applications of these techniques in industry.

The prediction of the solar irradiance is one of the key factor in Photovoltaic (PV) output systems. The first method for cloud cover detection and analysis was made by operators of meteorological stations using visual observations dividing the sky into eight parts (octas) for estimating the cloud coverage and based on the historical patterns they can check what kind of cloud is expect and what will be their projected output, however with high subjectivity [18]. Currently, the approach is being used as the basis of new technology as well. The positioning being used on the AI algorithms that do the work autonomously without any person being at the wheel.

Due to these uncertainties, since many years, several authors have found different methods for cloud cover estimation, like the use of all-sky cameras or, hereafter called, Hemispherical Sky Imagers (HSI). Within these camera methods, we can mention some as: threshold-based algorithm [19] and AI [23].

Many authors have used algorithm based of the RGB threshold of the sky image pixels as a metric for doing classification of clouds [19], [24], [25]. Cloud pixels are identified for high R and B values, while blue sky pixels have low R and high B values. However, this method has some difficulties to distinguish or detect clouds near the horizon and this method does not work optimally when the clouds are too close to the sun [26]. Other techniques within the same domain are the super pixel segmentation [27] algorithms, which are used to separate the cloud pixels from the rest of the picture. This algorithm divides the image into blocks [27] (or clusters) and the division is based mainly in the continuity of cloud contours, the texture and brightness of each pixel. Liu et al. [15] developed an automatic cloud detection algorithm using superpixel segmentation calculating the local threshold for each superpixel and then determining the threshold matrix for whole images. Furthermore, for cloud motion identification and forecast,

Scolari et al. [30] developed an algorithm based on all-sky images for prediction horizons in the range 1 to 10 minutes. The application of this technique is mainly used for cloud identification, cloud movement, and cloud forecast [31].

One of the promise techniques that is being used in this regard is the use of AI. AI has been used in different forecasting applications; solar irradiance being one of them. There are multiple forecasting techniques within AI, we will be looking at ANN and CNN as being the primary ones. This thesis will study these as potential techniques in the domain of solar irradiance forecasting.

Kamadinata et al. [34] created and contrasted two different ANN with first forecast cloud development heading where the result of this ANN is used as contribution for the second ANN for anticipating the worldwide level of the GHI. The results of this study showed a decrease of the computational exertion catching the pattern of the GHI quite well. Zhen et al. [35] proposed a cloud picture forecasting technique from all-sky pictures utilizing hereditary calculations following both the uprooting and misshape of cloud lessening the Euclidean distance in correlation with different strategies.

Convolutional neural networks (CNN) have been successfully applied to the classification and segmentation of regions of interest in images. As of 2017 and with the application of CNN in time series analysis, it is possible to promisingly predict forecast time series of more than one day. Due to the large number of works that have appeared in recent years [39] - [45], the prediction capacity of CNNs applied to image data for GHI prediction becomes evident. CNN have been applied and successfully used for cloud detection [87] and model cloud coverage estimations [47]. CNN were also programmed for forecasting more complex relationships [49] between variables with significant advantages for large images datasets [50]. In summary, the research interest in forecasting the GHI as output for PV components has increased due to recent changes in the energy sector.

Neural networks are likewise emphatically equipped for deciding the perplexing designs in information, functioning as a proficient device for reproduction of an uproarious framework driven by information, which is the reason they are appropriate for mind-boggling and variable time series forecasting. These are appropriate for demonstrating issues that require catching conditions and are equipped for saving information as they progress through the ensuing time steps in the information.

Hochreiter et al. [51] proposed a methodology for the expectation of sun-oriented irradiance utilizing profound intermittent neural networks fully intent on working on model intricacy and empowering highlight extraction of significant level elements. The proposed strategy showed preferable execution over the regular feedforward neural networks and backing vector machines.

The recurrent neural network (RNN) [52] design is an exceptional sort of ANN representing

information hub conditions by safeguarding successive data in an inward state, which permits the timelessness of information gathered from ensuing time steps. Be that as it may, the RNN is inclined to evaporating and detonating angles. This prompted the improvement of RNN variations like long transient memory (LSTM) networks [44], bidirectional LSTM, and gated repetitive units (GRU) as expansions of the RNN engineering by supplanting the traditional perceptron design with memory cell and gating systems that manage data stream across the network. These variations are generally utilized for the errand of sun-oriented irradiance forecasting.

There are many advantages to the AI algorithms, they are fast, not to complex and require a simple architecture. For example, Deep Learning (DL) takes away the simple structure to a much more complex structure which creates more complexity giving a better time series prediction analysis that would not be given anywhere.

Finally, Brockwell [53] is focused on the theory through DL, and thus, in the creation of better accuracy model and better time series in solar irradiance forecast.

3 Methods

This chapter conceptually explains working procedure of different meteorologic variables and also ANN and CNN. In 3.1. First, image processing is highlighted. The solar irradiance is explained in 3.2. ANN are explained in 3.3. Finally, CNN are explained in 3.4.

3.1 Image processing

To work with an image computationally it must be treated as a mathematical function. Each stored image possesses a finite amount of points and each of these points are indexed with natural values x, y annexed in the Cartesian plane.

Definition 3.1.1 (*Image*): An image is a function, $I : N \longrightarrow [0, 1]^c$.

where $N = [0, m - 1] \times [0, n - 1]$ represents the pixels, m and n represent the number of rows and columns, respectively. c is the number of channels. $c = 3$ represents the Red, Green and Bleu (RGB) channels.

In this work, the focus will be centered on the RGB images. Thus, the total number of available colors is $256 \times 256 \times 256$, or 16.777.216 possible colors. In addition, one of the most common operations within image processing and computer vision is the special filtering. The results for applying a linear filter H on an image X is a new image X' denoted by:

$$X'(u,v) = \sum_{(i,j)\in RH}^{n} X(u+i, v+j)H(i,j), \forall (u,v) \in RI$$

where RH and RI are the coordinates set for filter H and image X, respectively. This technique is used for noise elimination effects or for edge detection. In both cases, the new pictures obtained are completely dependent on the original pixels and their neighbours. For this reason, it is advisable to configure the information by matrices that consider which neighbours will or will not influence the determination of a new pixel.

3.2 Solar irradiance

Solar irradiance is the main influential component of solar power output. The combination of direct sunlight and cloud determines and influences surface solar irradiance.

According to Seckmeyer et al. [54] the Irradiance E is a receiver detector and defined as "radiance flux by a surface per unit area" and it is proportional to the square of the distance R from the radiator. This relationship is known as Photometric Distance's Law. In other words, Irradiance E that reaches an area A, decreases in proportion to the distance R between area A and radiation source S. The mathematical definition of E is:

$$E = \frac{d\phi}{dA_r},$$

where ϕ is the radiant flux and A_r is the area of the receptor (irradiated area). The unit of the irradiance is $W \cdot m^{-2}$.

3.3 Artificial neural networks

The artificial neural networks (ANN) are inspired from the natural neural network of the human nervous system. The theory of neural networks is based on the most important and most common cells in the brain, the neuron. Thanks to more than 86 billion neurons in our brain [55] we have a large number of synaptic connections which provide us with the ability to think. Each neuron receives information from approximately 10,000 other neurons. These neurons send pulses to hundreds or thousands of others simulating actions and reactions. Thus, an ANN can be considered as a mathematical model developed to emulate the human brain [49].

3.3.1 Components of an ANN

There are three basic elements of a neural model:

- **Set of synapsis:** a neuron is characterized by having a weight or a number. The input information x_j flows through connections that multiply it by a weight $w_{i,j}$. This product is the argument for a transfer function $\varphi(\cdot)$ that gives the output y_i. i represents the presynaptic neuron and j the postsynaptic neuron. Unlike the brain synapses in humans, the synaptic weights in an artificial neuron can be both negative and positive values.

- **Sum:** A linear operation will be the way in which the network adds the values of heavy entries for the respective synapse of the neuron.

- **Activation function:** To limit the amplitude of the outputs of the neurons, it is neces-

sary to consider an activation function.

The activation function $\varphi(\cdot)$ defines the output of a neuron in terms of the induction of the linear field y_i. The activation function calculates the state of activation of a neuron, transforming the global input into a state of activation. Therefore, the mathematical model of an ANN can then be written as follows:

$$u_i = \sum_{j=1}^{m} w_{i,j} x_j$$

and

$$y_i = \varphi(u_i + b_i)$$

where:

- $x_1, x_2, ..., x_m$ are the inputs
- $w_{i,1}, w_{i,2}, ..., w_{i,m}$ are the synaptic weights of neuron i
- u_i is the linear combination of the output expected by the inputs
- b_i represents the bias
- $\varphi(\cdot)$ is the activation function, and
- y_i is the output value of the neurons

The number of hidden neurons in a single hidden layer can be calculated by 3.1.

$$m = \sqrt{n+1} \pm \alpha, \tag{3.1}$$

where n is the number of inputs and l is the number of output neurons and α is a constant $(1 < \alpha < 10)$.

3.3.2 Transfer functions

As the biological neurons are active (excited) or inactive (non-excited), artificial neurons also have activation states. It is denoted by $\varphi(v)$ the activation function that defines the output of a neuron in terms of the induction of the linear field v. The activation function does nothing more than calculate the activation state of a neuron, transforming the global input (but not the threshold) into an activation value (state).

The most typical transfer functions are mathematically defined as:

- **Sigmoidal function (*sigmoid*):**

$$\varphi(v) = \frac{1}{1 + e^{-v\alpha}}$$

- **Hyperbolic tangent function (*tangh*):**

$$\varphi(v) = \frac{e^{\alpha v} - e^{-v\alpha}}{e^{\alpha v} + e^{-v\alpha}}$$

- **Rectified linear Unit (*ReLU*):**

$$f(v) = max(0, v)$$

where:

$$f(v) = \begin{cases} 0, & v < 0 \\ \\ v, & v \geq 0 \end{cases}$$

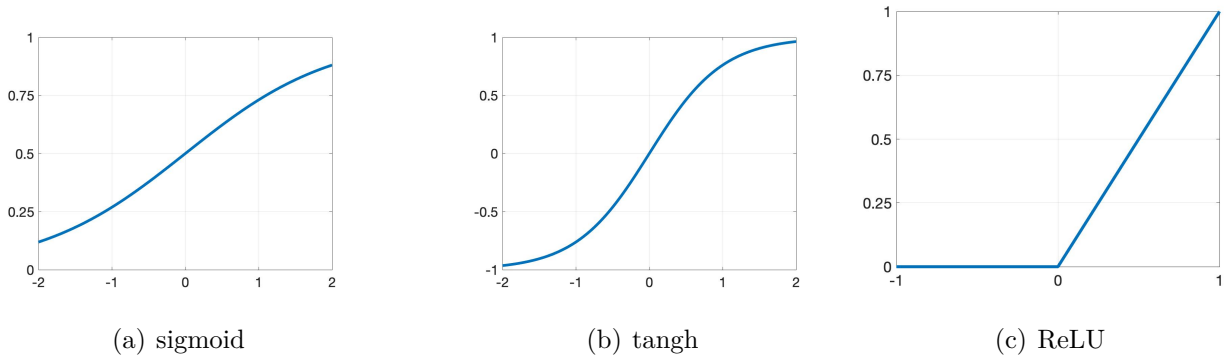(a) sigmoid   (b) tangh   (c) ReLU

Figure 3.1: Most commonly activation functions in artificial neural networks. (a) the sigmoidal function. (b) hyperbolic tangent function. (c) The rectified linear (ReLU) function.

The sigmoidal function is defined as strictly increasing and a great feature is that it exhibits linear and non-linear behavior and the output ranges of this function fall within a range from 0 to 1. A graph for $\alpha = 1$ is presented in Fig 3.1 (a). Another transfer function utilized in neural networks is the hyperbolic tangent function. It assumes the values -1 or 1. This function takes the input values, which can range between plus and minus infinity. Fig 3.1 (b) show a graph for the hyperbolic tangent function with $\alpha = 1$. The Rectified Linear Unit (*ReLU*) transfer function increases the chances of convergence of the network causing the no-saturation of neurons, and thus, *ReLU* allows the network to learn more quickly and efficiently, due to

the vanishing gradient problem [56]. If the input value (x) in Fig. 3.1 (c) is negative, then the value will replace to zero, otherwise, the value is returned. This function is one of the most used because it allows very fast learning in neuronal networks.

3.3.3 Backpropagation

The way how neurons in an ANN operate and interact is directly related to the algorithm used for training, i.e. the learning algorithm. Before starting the training, the architecture of the neural network must be defined and initialized with random weights. During training, the connection's weights are adapted based on the error between the desired computational output. This process is repeated again and again until a minimum (and acceptable) error is reached. Thus, the loss function, which is responsible for measuring desired and computational error must be determined. The most used functions are defined below:

- **Mean squared error (MSE):**

$$MSE = \frac{1}{n} \sum_{i=1}^{n} (y_i - x_i)^2$$

- **Mean absolute error (MAE):**

$$MAE = \frac{\sum_{i=1}^{n} |y_i - x_i|^2}{n}$$

- **Mean absolute percentage error ($MAPE$):**

$$MAPE = \frac{100}{n} \sum_{i=1}^{n} \frac{(y_i - x_i)}{y_i}$$

where n is the data points on all variables, y_i are the observed values and x_i are the predicted value, and thus, the output error settings are based on the loss functions chosen for training.

One of the most utilized learning algorithms to train a network is the Backpropagation algorithm. This algorithm, introduced by Rumelhart et al. [71], considers a differentiable error function to minimize with activation functions of the neuron. Backpropagation changes the network's weights so that it can produce a desired output for a particular input, i.e., it learns by example, and thus, Backpropagation works with an error function. The error of the output in the jth neuron in the nth iteration will define as:

$$e_j(n) = d_j(n) - y_j(n)$$

where the neuron j corresponds to the output. z_i will denote the output of the neuron i, and thus,

$$a_j = \sum_i w_{ji} z_i$$

is what receive the neuron j. Now, we will denote $E^l = E(y^l) = E(y_1^l, y_2^l, ..., y_p^l)$ the error of the network with respect to the vector y^l with input x^l, $\forall l = 1, 2, ..., m$. Thus, the total error of the network is:

$$E = \sum_{l=1}^{m} E^l$$

The Backpropagation algorithm consists of two steps. The first is to determine the partial derivatives $\frac{\varphi E^l}{\varphi w_{ji}}$ and the second is to use this information to update the weights. Partially deriving we obtain:

$$\frac{\varphi E^l}{\varphi w_{ji}} = \frac{\varphi E^l}{\varphi a_j} \frac{\varphi a_j}{\varphi w_{ji}} = \delta_j^l z_i$$

where $\delta_j^l = \frac{\varphi E^l}{\varphi a_j}$ and $\delta_j^l z_i$ correspond to a neuron of the output layer.

In the second step, a rule of variation of the weights of the network must be chosen as a function of the partial derivatives $\frac{\varphi E^l}{\varphi w_{ji}}$. The classic way is to use the method of the descent of the gradient:

$$\Delta w = -\eta \Delta E;$$

with $\eta > 0$ and $\Delta E = \frac{\varphi E}{\varphi w_{ji}}$.

In words, once the stimulus has been applied to the inputs, it spreads from the first layer through the next layers of the network, until it generates an output. The output signal is compared to the desired output and, with this way, an error signal is created. Kramer et al., [72] have described the convergence of the Backpropagation algorithm as: " . . . having converged when the absolute rate of change in the average squared error per epoch is sufficiently small".

Then, the error outputs are propagated backwards starting with the output layer to the neurons of the hidden layer(s) where the importance of these neurons is the direct contribution to the output of the network. The neurons of the hidden layers receive only a small fraction of the error signal. This process is repeated layer by layer until all the neurons have received an error signal that describes their contribution to the total network error. Rojas [73] defines the Backpropagation algorithm as a combination of the weights of the networks that minimizes the calculation's error.

The aim of this process is that as the network trains, the neurons of the hidden layers are organized so that they learn to recognize special characteristics of the total input space. After

the training, when presenting an arbitrary input pattern (noise or incomplete information) the neurons of the hidden layers will respond with an active output if the pattern presented is not too different from the training. In this way, the network trains and goes on storing information to deliver the best output.

The discovery of the Backpropagation algorithm led to the widespread use of Fourier transforms that is used in a wide range of practical applications.

3.3.4 Selection of the network

The practical management of neural networks has shown that the number of inputs and outputs are inevitable parameters. Thus, all other network parameter are variables. in addition to the number of neurons and layers, the configuration of the initially chosen weights has a significant influence on the network. Thus, for this work, different neural networks were configured. Each one differs in its construction form, initial values and in the learning algorithm.

The provision of an objective evaluation criterion for the election of the "best" network is extremely difficult. For this reason, the technique used in all the networks built was to add hidden layers and in these to add neurons. The idea is to achieve the desired result with the least number of hidden layers possible and at the same time with the least number of neurons in each of these layers. Thus, the interaction of the data decides the quality of the test. The criteria for choosing a network was that both the $RMSE$ and the MAE are minimized as much as possible.

3.4 Convolutional neural networks

Convolutional neural networks (CNN) have drastically broadened the potential of computational models to represent data of multiple levels of abstraction [57]. In the field of solar energy, CNNs have been used for several applications such as classification, cloud detection, segmentation and image reconstruction [58] - [59]. CNN architectures consist of multiple layers of convolutional filters of one or more dimensions. After each processed convolutional layer, a non-linear function is added to perform causal mappings [60].

A convolutional operator is a process where it will be taken a small matrix of kernel (or filter) being passed over an image and transform it based on the values from filter. Thus, each output of a convolutional layer is calculated as follows:

$$y_j = g(b_j + \sum_i^N K_{i,j} \otimes Y_i)$$

where Y_i is the output matrix of the previous layers, $K_{i,j}$ is the convolutional kernel of these

connections, b_j is a threshold and $g(.)$ is a non-linear activation function. Thus, y_j is the final response of the linear combination between Y_i and $K_{i,j}$ of the neuron j.

The interest of reducing the volume of data is very important for computational costs. CNNs utilize pooling layers to reduce complexity through dimension reduction. This task is carried out in a certain way interacting within the network and doing operations in small regions of the matrix of input, accumulating the elements of the feature layers. Thus, the definitions of a pooling layer $P_{i,j}$ can be defined as:

$$P_{i,j} = maxA[p(i-1) + m, p(j-1) + n],$$

where $n, m = 1, ..., k$. $A_{n \times n}$ is a matrix. k is the amplitude and p is the stride.

The architecture of a convolutional neural network begins with the interaction of a convolutional layer and a pooling layer. This process continues repeatedly until a set of matrices is obtained. Finally, when all the elements are expressed as a vector (favoring process) these elements are taken as inputs to the neural network with a low computational cost compared to the initial matrices. Three characteristics distinguish CNN from full connected neural networks: sparse interactions between the neurons, equivariant representations and the sharing of parameters, and thus, CNNs are suitable for image processing.

4 Published articles of this cumulative thesis

4.1 Autoregressive Neural Network for Cloud Concentration Forecast from Hemispheric Sky Images

4.1.1 Declaration of contributions

I and Gunther Seckmeyer perceived the idea to accurately determine from all-sky images how many clouds (%) are moving in the direction of the sun in the next few minutes using artificial neural networks. I programmed all programs and created all visualizations. All authors contributed substantially with comments and revised the manuscript.

4.1.2 Published article

Cristian Crisosto, Autoregressive Neural Network for Cloud Concentration Forecast from Hemispheric Sky Images. *International Journal of Photoenergy, vol. 2019, Article ID 4375874, 8 pages, 2019. https://doi.org/10.1155/2019/4375874.*

Research Article

Autoregressive Neural Network for Cloud Concentration Forecast from Hemispheric Sky Images

Cristian Crisosto (ID)

Leibniz Universität Hannover, Institute for Meteorology and Climatology, Herrenhäuser Straße 2, 30419 Hannover, Germany

Correspondence should be addressed to Cristian Crisosto; crcrisos@gmail.com

We present here a new method to predict cloud concentration five minutes in advance from all-sky images using the Artificial Neural Networks (ANN). An autoregressive neural network with backpropagation (Ar-BP) was created and trained with four years of all-sky images as inputs. The pictures were taken with a hemispheric sky imager fixed on the roof at the Institute of Meteorology and Climatology (IMUK) of the Leibniz Universität Hannover, Hannover, Germany. Firstly, a statistical method is presented to obtain key information of the pictures. Secondly, a new image-processing algorithm is suggested to optimize the cloud detection process starting with the Haze Index. Finally, the cloud concentration five minutes in advance at the IMUK is forecasted using machine learning methods. A persistence model forecast to provide a reference for comparison was generated. The results are quantified in terms of the root mean square error (RMSE) and the mean absolute error (MAE). The new algorithm reduced both the RMSE and the MAE of the prediction by approximately 30% compared to the reference persistence model under diverse cloud conditions. The new algorithm could be used as a tool for the stable maintenance of the network for the transmission system operators, i.e., the primary control reserve (within 30 seconds) and the secondary control reserve (within 5 minutes).

1. Introduction

Changes in the solar irradiance dynamic are significantly impacted by clouds, which makes it difficult to achieve accurate PV power forecasting [1, 2]. With a reliable cloud performance forecast, uncertainty in the solar irradiance prediction can be minimized and optimized. Increased electricity demand requires balancing energy. In this case, the grid operator needs additional power supply to his grid at short notice. The prequalification requirements in German markets provide that a complete deployment of primary control reserve has been completed within 30 seconds and the secondary control energy must be available in full within five minutes [3]. Quaschning [4] shows the importance of the energy control for the first 15 seconds, 30 seconds, 1 minute, 5 minutes, 15 minutes, and 60 minutes when, for example, the current reserve is running low. Thus, a prediction of the cloud concentration for the next five minutes, for solar radiation forecast, makes an important contribution to the

efficient and economical application for many areas of solar energy use. Solar irradiance is the key factor for solar photovoltaic (PV) generation. The International Energy Agency estimates that after 2060, solar energy could cover up to a third of the world's energy consumption. Therefore, the solar energy use is likely to grow by a double digit rate throughout the world and for decades.

Thus, solar power will be an important contributor to the future power supply technologies, influencing the planning, profitability, and operation of power systems. For stabilizing the fluctuations in the energy output of PV plants, the impact of clouds must be considered to achieve a sustainable, affordable, and reliable electricity supply [5].

All-sky images have already been proven to achieve an efficient observation from the ground delivering a comprehensive view for kilometers [6]. The application of this technique is mainly used in the solar forecasting for cloud identification, cloud movement, and cloud forecast [7]. Many authors use algorithms based on a red/blue threshold of the

RGB channels of all-sky images for cloud classification [8]. However, this method is unable to detect thin clouds near the horizon [9].

Additionally, several studies report different ways for identifying clouds and predicting their future movements in a more objective manner. Many authors report methods in cloud identification using a threshold and segmentation of the pictures. Liu et al. [10] developed an automatic cloud detection algorithm using superpixel segmentation calculating the local threshold for each superpixel and then determining the threshold matrix for whole images. Scolari et al. [11] developed a cloud motion identification algorithm based on all-sky images for prediction horizons in the range 1 to 10 minutes.

More recently, Crisosto et al. [12] developed an algorithm to predict the global horizontal irradiance (GHI) one hour in advance from all-sky images using the ANN. This study reduced both the RMSE and the MAE of the one-hour prediction by approximately 40% of the forecast prediction compared to the reference persistence model subdividing the all-sky images into concentric circles to be able to simulate more accurately the GHI.

Different methodologies utilizing two ANN have already been employed. Kamadinata et al. [13] developed and compared two different ANN to first forecast cloud movement direction where the output of this ANN is utilized as input for the second ANN for predicting the GHI. The results of this study show a reduction of the computational effort capturing the trend of the GHI very well. Zhen et al. [14] proposed a cloud image forecasting method from all-sky images using genetic algorithms tracking both the displacement and deformation of cloud reducing the Euclidean distance in comparison with other methods.

Therefore, in order to support accurate solar irradiance forecasts, we propose a cloud concentration forecast algorithm using the artificial neural networks (ANN), which can be later used as a tool for solar energy forecasts. Section 2 briefly describes the data and image acquisition. Section 3 describes the methodologies necessary for this study. The forecasting results are given in Section 4. Finally, in section 5, the conclusions and future work will be discussed.

2. Data

The main component of solar power output is the solar irradiance, which under the presence of clouds is extremely affected. Thus, cloud motion becomes the key element of solar power output.

2.1. Image Acquisition. The camera system is installed inside a weatherproof housing on the roof of the Institute of Meteorology and Climatology (IMUK) of the Leibniz Universität Hannover, Hannover, Germany. The pictures were recorded with a Canon EOS 700D equipped with a Dörr DHG fisheye lens providing a 183° field of view. The exposure time of the pictures was 1000/s. All time hours are expressed in coordinated universal time (UTC).
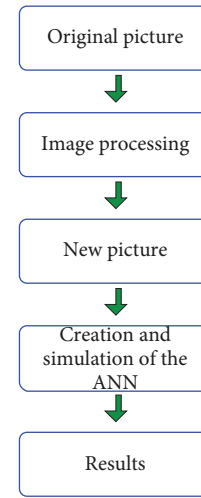

Figure 1: Cloud movement process with ANN.

3. Methodology

We developed an algorithm to forecast cloud concentration five minutes in advance from all-sky images using the ANN. We can divide the new algorithm in two main steps. The first part highlights the image-processing algorithm for extracting parameters from all-sky images. The second step comprises the ANN method. Figure 1 shows the cloud recognition and cloud concentration forecast with ANN.

3.1. Cloud Pixel Identification. Clear sky is characterized by high blue pixel intensity and low red pixel intensity, while thick cloud pixels are characterized by high intensity in both channels. Thus, the cloud identification algorithm determines if a pixel corresponds to a cloudy point or clear sky. To surpass the limitations of using only the blue and red RGB channels, we used a cloud identification method which also uses green. This color discrimination method is simple and distinguishes cloud from blue sky by the ratio of the counts of red, green, and blue color in each pixel. Using the Sky Index (equation 1) method by Yamashita et al. [15] and refining its uncertainties, we calculated the Haze Index (equation 2) as detailed by Schrempf [16] to expand (1) for a better cloud identification.

$$\text{Sky Index} = \frac{\text{count}_{\text{blue}} - \text{count}_{\text{red}}}{\text{count}_{\text{blue}} + \text{count}_{\text{red}}}, \tag{1}$$

$$\text{Haze Index} = \frac{((\text{count}_{\text{red}} + \text{count}_{\text{blue}})/2) - \text{count}_{\text{green}}}{((\text{count}_{\text{red}} + \text{count}_{\text{blue}})/2) + \text{count}_{\text{green}}}. \tag{2}$$

The total cloud area was then calculated by the separation of cloud and sky done by the Haze Index in the all-sky image. To avoid oversaturated pixels, the percentage of clear sky and cloud cover is obtained without considering the sun's circumference. The extraction of the
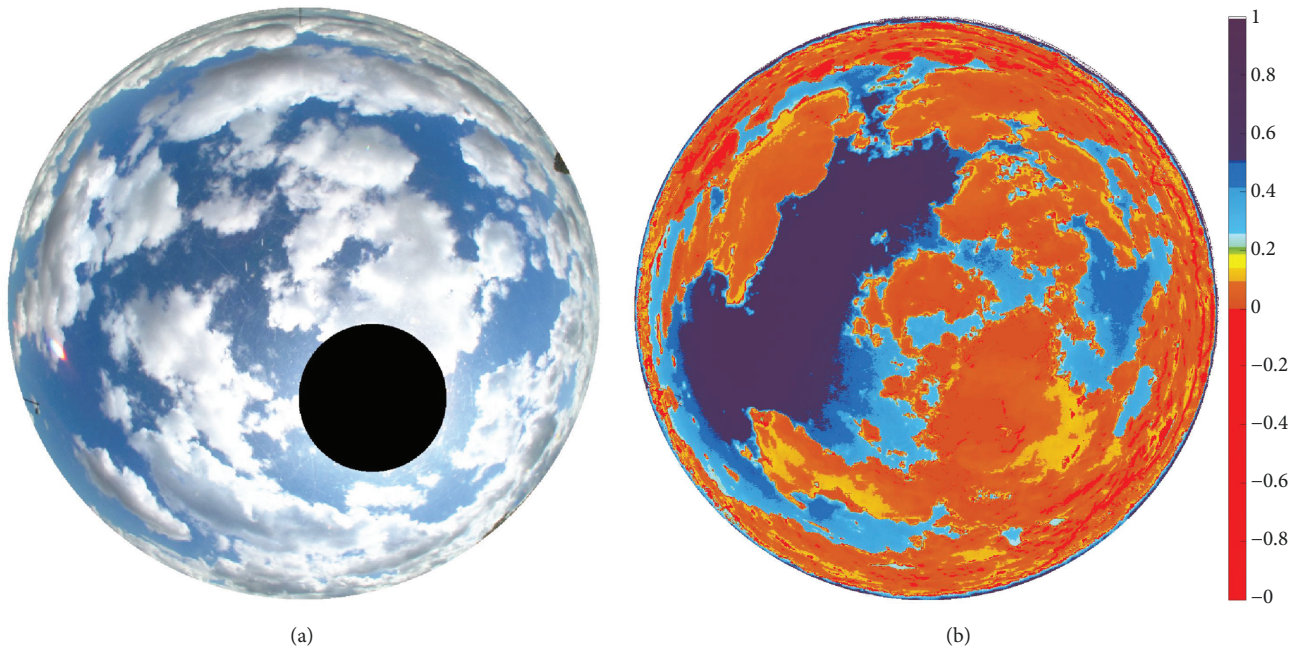
(a)

(b)

FIGURE 2: (a) Cropped black area and coverage of the sun from the original picture. (b) Haze Index image.

statistical information from all pictures was limited to the sun's zenith angle of 70°. Figure 2 shows the Haze Index image processing.

3.2. Setup of the ANN. The algorithm used seven inputs and one output. For the final configuration of the ANN see Table 1. The inputs x_j flow through the next layer multiplying their values by a weight $w_{i,j}$, while the resulting product is used as argument for a transfer function f giving the output y_i. i represents the presynaptic neuron and j the postsynaptic neuron, see equation 3 and equation 4. The quantity of hidden neurons per single hidden layer was calculated by (5).

$$u_i = \left(\sum_{j=1}^{n} w_{i,j} x_j \right), \tag{3}$$

$$y_i = f(u_i + b_i), \tag{4}$$

where x_j is the input, w_i is the synaptic weight, u_i is the linear combination of the inputs, b_i is the bias, f is the activation function, and y_i is the output.

$$m = \sqrt{n+1} \pm \alpha, \tag{5}$$

where n is the number of inputs and l is the number of output neurons. α is a constant $(1 < \alpha < 10)$.

The build of neural networks has shown that in addition to the number of neurons and layers, the configuration of the initially chosen weights has a significant influence on the network. Thus, different neural network structures were configured to carry out this job. Each one differs in its construction form, initial values, and learning algorithm.

TABLE 1: The neural network structure occupied in this investigation.

Input	Hidden layers	Neurons in the first hidden layer	Neurons in the second hidden layer	Output
7	2	4	2	1

The selection of the "best" network was extremely difficult. For this reason, the technique used in all the networks built was to add hidden layers and in these to add neurons. The idea is to achieve the desired result with the least possible number of hidden layers and neurons in each of these layers.

The interaction of the data decides the quality of the test. The criteria for choosing a network was that both the RMSE and the MAE were minimized as much as possible.

3.3. Cloud Concentration Forecasting. To accurately follow cloud concentrations five minutes in advance, we created the ring program, see Figure 3. The ring program divides the pictures in concentric rings with the sun as their center. We can see in the picture the subdivision of n concentric rings. Each of these rings represents a temporal resolution. The width depends on the distance from the horizon to the center of the sun due to the equidistant projection. Figure 3(a) shows the number of circles on 22nd June 2014 at 12:51 over the original picture, and Figure 3(b) shows the rings at the same time over the Haze Index image. The number of circles in this moment of the day was $n = 10$ that corresponds to approximately 10 minutes of future information, i.e., the time that the clouds could take to reach the center of the sun. In addition, the wind speed is also measured at the IMUK, and each picture is stored with the
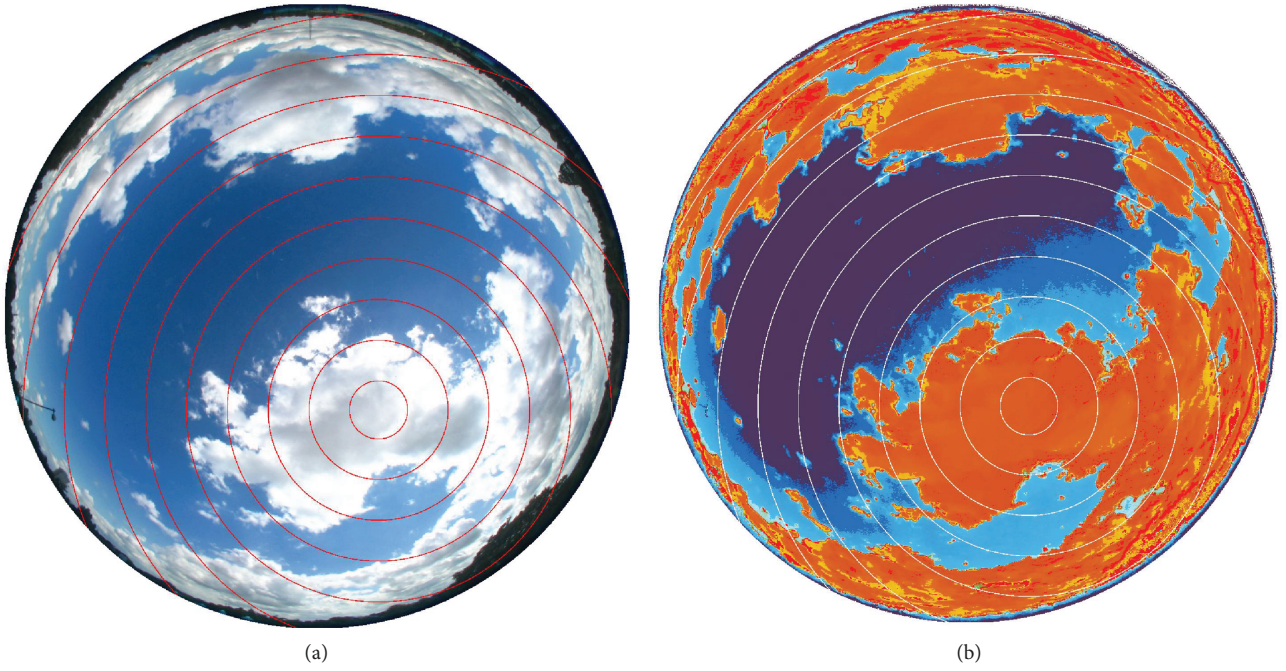
(a)

(b)

FIGURE 3: (a) shows the 10 circles on 22nd June 2014 at 12:51 on the original image. (b) shows 10 circles on 22nd June 2014 at 12:51 on the Haze Index image.

corresponding wind speed to estimate how many circles there should be in each picture.

In the training phase of the ANN, we used the percentage of cloud in each ring, the sun zenith angle (SZA) and the mathematical standard deviation, mode, median, and average of the RGB channels of each ring at the time t as input parameters. One-minute ahead cloud cover fraction of the next ring at $t + 1$ of the next picture is the output of the program. Now, to predict the cloud concentration at time $t + 2$, we take all inputs from the time t with exception of the cloud cover; this input is taken at time $t + 1$.

For example, on 22nd June 2014, the simulation started at 12:51 (t) and estimated the cloud cover fraction of the next ring of the next picture at 12:52 ($t + 1$) (Figures 4(a) and 4(b)). Subsequently, to forecast the cloud cover fraction of the next ring at 12:53 ($t + 2$), we used all input parameters of the circle at 12:51 (t) with exception of the input cloud cover, which was taken from the forecasted cloud cover of 12:52 ($t + 1$). The idea is to use the information of only one picture to forecast the cloud cover from 1-5 minutes ahead, completing all 5 rings.

Therefore, the ANN analyzed the actual cloud concentration at the current ring in order to know if one minute in advance, the next ring will have the same, larger, or smaller cloud concentration. This information could be important to know the most likely cloud concentration near the sun at the next minutes, in order to know how variable the solar irradiance will be in this time frame.

4. Results

To evaluate the proposed method, the first five minutes from 50 images with different cloud concentrations and sun positions were manually selected and analyzed. The selected days represent high cloud variability, i.e., a high variability of solar irradiance. The RMSE (6), the MAE (7), and the coefficient of determination (R^2) (8) were used to evaluate the performance of the new model for these five minutes. To finally validate our model, the statistical sampling (9) was utilized and the results are presented as a boxplot. The mathematical definitions of the statistical procedure are expressed as follows:

$$\text{RMSE} = \sqrt{\sum_{i=1}^{N} \frac{\|y_i - x_i\|}{N}}, \tag{6}$$

$$\text{MAE} = \frac{\sum_{i=1}^{N} |y_i - x_i|}{N}, \tag{7}$$

$$R^2 = \frac{\sum_{i=1}^{N} (y_i - \bar{y})(x_i - \bar{x})}{\left[\left(\sum_{i=1}^{N} (y_i - \bar{y})^2\right)\left(\sum_{i=1}^{N} (x_i - \bar{x})^2\right)\right]^{1/2}}, \tag{8}$$

where y_i was the forecast value, x_i was the measured value, and N was the number of samples. Additionally, $\bar{x} = \sum_{i=1}^{N} x_i$ and $\bar{y} = \sum_{i=1}^{N} y_i$.

$$x = \frac{Z^2 N p q}{e^2 (N-1) Z^2 p q}, \tag{9}$$
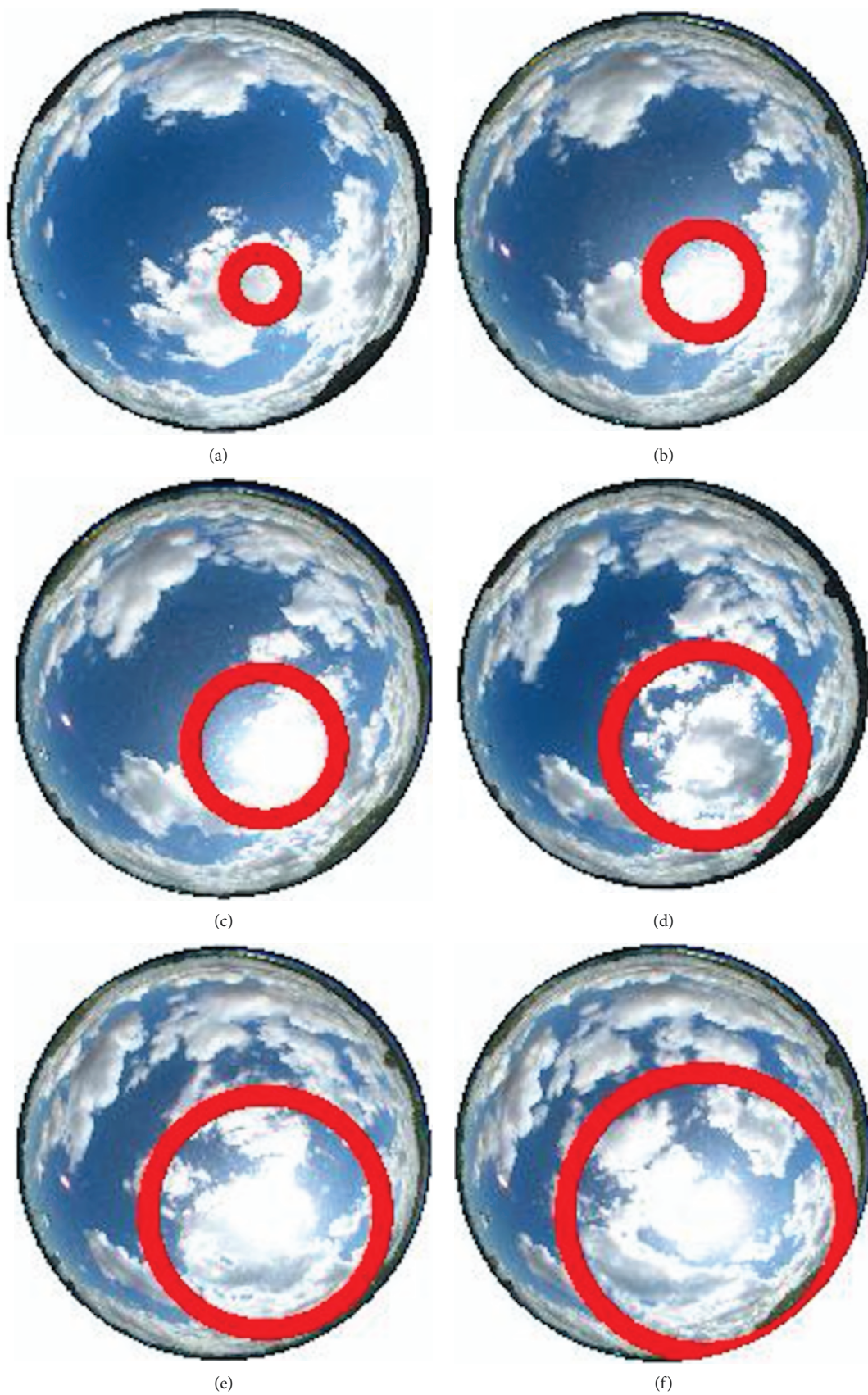
(a)

(b)

(c)

(d)

(e)

(f)

FIGURE 4: Observation of all-sky images on 22nd June 2014. The red circle in (a) corresponds at 12:51. (b) at 12:52. (c) at 12:53. (d) at 12:54. (e) at 12:55. (f) at 12:56.
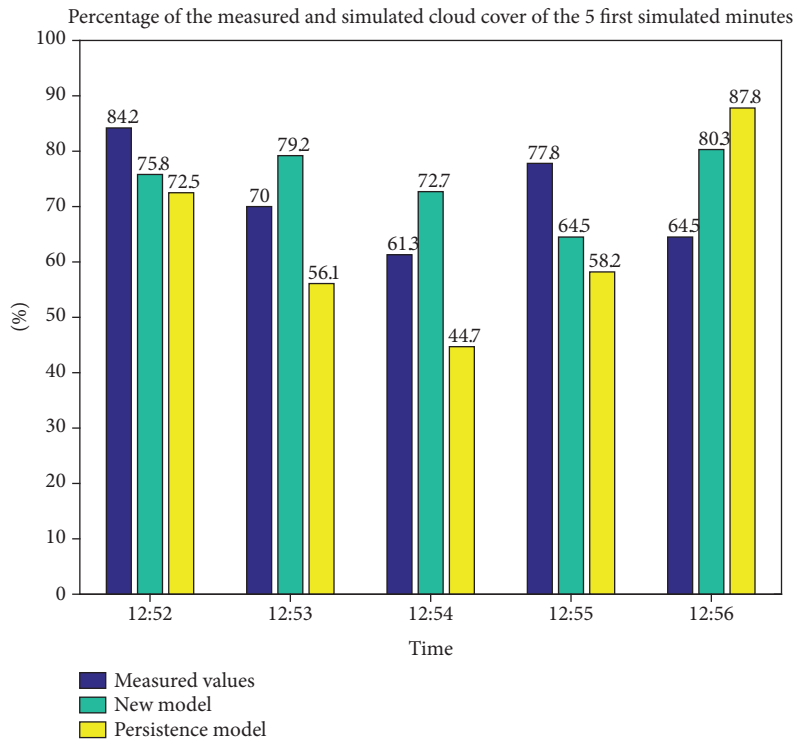
FIGURE 5: Comparison between the measured and simulated cloud cover on 22nd June 2014 from 12:52 until 12:56.
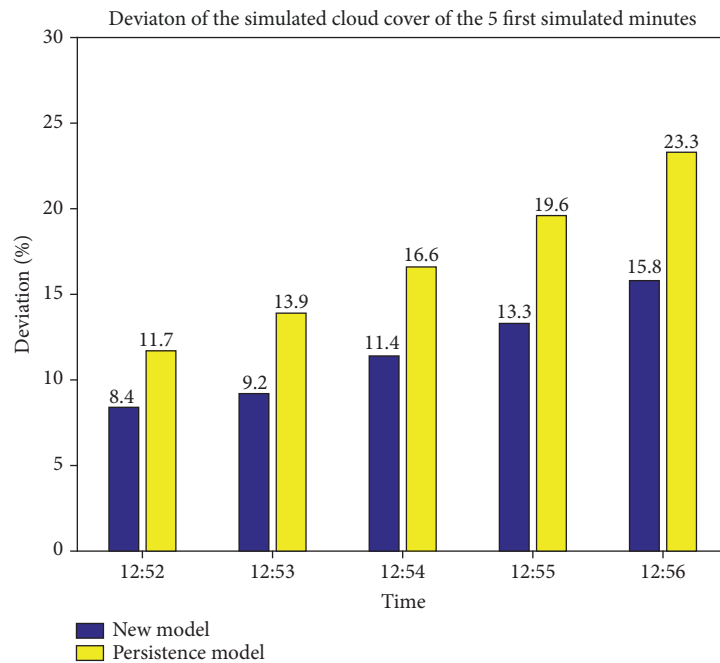

FIGURE 6: Deviation between the simulated cloud cover of the new model and the persistence model on 22nd June 2014 from 12:52 until 12:56.

where N was the total of the set, $p = 0.95$, $q = 0.05$, and $Z = 1.96$ (this value corresponds to the confidence level of 95%).

The new algorithm was compared with the benchmark algorithm, the persistence model. This model is the simplest forecasting model and can be remarkably good for short-term horizons [17]. This model is the most common reference model for short forecasting term of solar irradiance [18].

4.1. Analysis of a Case on 22nd June 2014. Now, we present an example of the simulated results on 22nd June 2014 from 12:52 until 12:56 using the new algorithm. The deviation

TABLE 2: Statistic indicator comparison between the new ANN forecast model and the persistence forecast model for the 50 manually selected pictures.

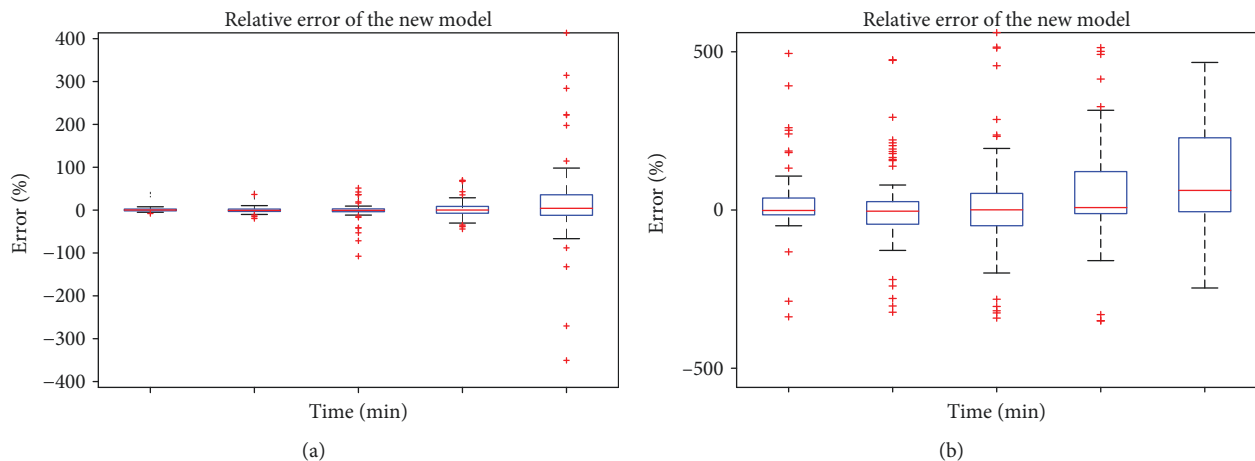| Simulation's time	Model	RMSE (cloud amount)	MAE (cloud amount)	R^2
5 minutes (from 145 different pictures)	ANN	51	43	0.96
	Persistence	70	61	0.79

FIGURE 7: Relative deviation as boxplot for the first five minutes. (a) corresponds to the new ANN. Here, we can see that the deviations are narrower concentrated in the middle interquartile ranges. (b) corresponds to the persistence model. 50% of the deviations are not exactly located in the middle. In addition, the 25% and 75% of the deviation is higher than in (a).

between the measured cloud concentration at time $t + 1$ and the simulated cloud concentration at time $t + 1$ was calculated according to equations 6 and 7. The new algorithm produced a high-quality forecast compared to the reference persistence model.

The measured cloud concentration at 12:52 was 84.2%, and our algorithm simulated 75.8%, i.e., a difference of 8.4%, while the persistence model had a difference of 11.7%. For the next minute simulation (at 12:53), our model simulated 79.2% of the total cloud concentration and the measured value was 70.0% resulting in a deviation of 9.2%. Here, the persistence model difference is 13.9%. Figure 5 shows the measured cloud concentration of the first five minutes and the simulated cloud concentration for the new algorithm and the persistence model.

It is also worth mentioning that forecasting with images completely covered with gray and dark gray clouds is of minor relevance for solar energy forecast. Hence, images with a solar global irradiance smaller than $100 \, \text{W/m}^2$ were not used in this work. Figure 6 shows the total deviation of both models.

Table 2 presents a comparison between the results of the different methods. Over 5 months of validation periods, we got 240 valid cases. However, not every picture was considered for validation. Full cloudy pictures (stratus cloud) and when the clouds did not have a form (shape) to be followed were not considered. Thus, only pictures with defined clouds (cumulus cloud) were considered for validation. To validate our algorithm, we applied statistical samplings. Therefore,

taking into consideration a confidence level of 95%, with a margin of error of 6%, our simulated cases were 145.

Therefore, applying the new ANN model to the 145 pictures, the presented model achieved an average of 30% for all sky conditions compared with the persistence model. Unfortunately, direct comparisons with other methods are difficult due to different time horizons and regional weather conditions.

Figure 7 shows the relative deviations as boxplots. The results suggest that the new model (Figure 7(a)) shows a symmetrical approach for the 50% sample rate. In addition, Figure 7(b) shows an asymmetrical distribution of outliers and a decreasing number of outliers, which leads to higher uncertainties. In conclusion, the uncertainty of the new model increased, but not as abruptly as with the persistence model, when more simulated data are introduced.

5. Conclusions

A new algorithm to forecast cloud distribution five minutes in advance has been presented. The model presented here combines all-sky images and an Ar-BP ANN. The cloud pixels were identified with the help of the Haze Index. The methodology described here only needs one all-sky image for predicting cloud concentration one minute ahead. According to the simulation results, our model makes a significant progress to predict cloud concentration five minutes in advance using a machine learning method, outperforming the persistence model. This method has already been

successfully tested as a tool as an important step for predicting the GHI one hour in advance [12]. The horizon time prediction of the new forecasting model can play an important role in German markets and within the European Union as well.

Future work will expand this methodology for forecasting the full image for longer periods, maybe using satellite information. In addition, the idea is to extend the proposed methodology to collect universally high-quality data giving a more robust validation.

Data Availability

The data used to support the findings of this study are ?available from the corresponding author upon request.

Conflicts of Interest

The authors declare that they have no conflicts of interest.

Acknowledgments

References

[1] A. T. Lorenzo, W. F. Holmgren, and A. D. Cronin, "Irradiance forecasts based on an irradiance monitoring network, cloud motion, and spatial averaging," *Solar Energy*, vol. 122, pp. 1158–1169, 2015.

[2] F. Wang, Z. Zhen, Z. Mi, H. Sun, S. Su, and G. Yang, "Solar irradiance feature extraction and support vector machines based weather status pattern recognition model for short-term photovoltaic power forecasting," *Energy and Buildings*, vol. 86, pp. 427–438, 2015.

[3] https://www.bundesnetzagentur.de/DE/Sachgebiete/Elektrizit aetundGas/Unternehmen_Institutionen/Versorgungssicherhe it/Engpassmanagement/Regelenergie/regelenergie-node.html.

[4] V. Quaschning, "Statistiken," 2017, https://www.volker-qu aschning.de/datserv/pv-welt/index.php.

[5] IEA, *International Energy Agency, World Energy Outlook 2016, Executive Summary*, International Energy Agency, World Energy Outlook, 2016, http://www.iea.org/publications/free publications/publication/WEB_WorldEnergyOutlook2015Ex ecutiveSummaryEnglishFinal.pdf.

[6] D. Bernecker, C. Riess, E. Angelopoulou, and J. Hornegger, "Continuous short-term irradiance forecasts using sky images," *Solar Energy*, vol. 110, pp. 303–315, 2014.

[7] R. Marquez and C. F. M. Coimbra, "Intra-hour DNI forecasting based on cloud tracking image analysis," *Solar Energy*, vol. 91, pp. 327–336, 2013.

[8] J. Yang, W. Lu, Y. Ma, and W. Yao, "An automated cirrus cloud detection method for a ground-based cloud image," *Journal of Atmospheric and Oceanic Technology*, vol. 29, no. 4, pp. 527–537, 2012.

[9] A. Cazorla, F. J. Olmo, and L. Alados-Arboledas, "Development of a sky imager for cloud cover assessment," *Journal of the Optical Society of America A*, vol. 25, no. 1, pp. 29–39, 2008.

[10] S. Liu, L. Zhang, Z. Zhang, C. Wang, and B. Xiao, "Automatic cloud detection for all-sky images using superpixel segmentation," *IEEE Geoscience and Remote Sensing Letters*, vol. 12, no. 2, pp. 354–358, 2015.

[11] E. Scolari, F. Sossan, and M. Paolone, "Irradiance prediction intervals for PV stochastic generation in microgrid applications," *Solar Energy*, vol. 139, pp. 116–129, 2016.

[12] C. Crisosto, M. Hofmann, R. Mubarak, and G. Seckmeyer, "One-hour prediction of the global solar irradiance from all-sky images using artificial neural networks," *Energies*, vol. 11, no. 11, article 2906, 2018.

[13] J. O. Kamadinata, T. Lit Ken, and T. Suwa, "Global solar radiation prediction methodology using artificial neural networks for photovoltaic power generation systems," in *Proceedings of the 6th International Conference on Smart Cities and Green ICT Systems - Volume 1: SMARTGREENS*, Porto, Portugal, 2017.

[14] Z. Zhen, Z. Wang, F. Wang, Z. Mi, and K. Li, "Research on a cloud image forecasting approach for solar power forecasting," *Energy Procedia*, vol. 142, pp. 362–368, 2017.

[15] M. Yamashita, M. Yoshimura, and T. Nakashizuka, "Cloud cover estimation using multitemporal hemisphere imageries," *International Archives of the Photogrammetry, Remote Sensing and Spatial Information Science*, vol. 35, pp. 826–829, 2004.

[16] M. Schrempf, *Entwicklung eines Algorithmus zur Wolkenerkennung in Digitalbildern des Himmels*, Diploma Thesis at IMuK, 2012.

[17] D. S. Wilks, *Statistical Methods in the Atmospheric Sciences*, Academic Press, Cambridge, MA, USA, 2011.

[18] M. P. Almeida, O. Perpiñán, and L. Narvarte, "PV power forecast using a nonparametric PV model," *Solar Energy*, vol. 115, pp. 354–368, 2015.

4.2 One-Hour Prediction of the Global Solar Irradiance from All-Sky Images Using Artificial Neural Networks

4.2.1 Declaration of contributions

Gunther Seckmeyer perceived the idea to determine the irradiance from all-sky images using artificial neural networks. Together with Martin Hofmann and Riyad Mubarak I created the drafts for this article. I programmed all programs and created all visualizations. All authors contributed substantially with comments and revised the manuscript.

4.2.2 Published article

One-Hour Prediction of the Global Solar Irradiance from All-Sky Images Using Artificial Neural Networks

Cristian Crisosto [1],*, Martin Hofmann [1,2] , Riyad Mubarak [1] and Gunther Seckmeyer [1]

[1] Institute for Meteorology and Climatology, Leibniz Universität Hannover, Herrenhäuser Straße 2, 30419 Hannover, Germany; martin.hofmann@valentin-software.com (M.H.); mubarak@muk.uni-hannover.de (R.M.); seckmeyer@muk.uni-hannover.de (G.S.)

[2] Valentin Software GmbH, Stralauer Platz 34, 10243 Berlin, Germany

* Correspondence: crcrisos@gmail.com; Tel.: +49-511-762-4453

Abstract: We present a method to predict the global horizontal irradiance (GHI) one hour ahead in one-minute resolution using Artificial Neural Networks (ANNs). A feed-forward neural network with Levenberg–Marquardt Backpropagation (LM-BP) was used and was trained with four years of data from all-sky images and measured global irradiance as input. The pictures were recorded by a hemispheric sky imager at the Institute of Meteorology and Climatology (IMuK) of the Leibniz Universität Hannover, Hannover, Germany ($52.23°$ N, $09.42°$ E, and 50 m above sea level). The time series of the global horizontal irradiance was measured using a thermopile pyranometer at the same site. The new method was validated with a test dataset from the same source. The irradiance is predicted for the first 10–30 min very well; after this time, the length of which is dependent on the weather conditions, the agreement between predicted and observed irradiance is reasonable. Considering the limited range that the camera and the ANN can "see", this is not surprising. When comparing the results to the persistence model, we observed that the forecast accuracy of the new model reduced both the Root Mean Square Error (RMSE) and the Mean Absolute Error (MAE) of the one-hour prediction by approximately 40% compared to the reference persistence model under various weather conditions, which demonstrates the high capability of the algorithm, especially within the first minutes.

Keywords: solar energy; all-sky image; solar irradiance prediction; artificial neural networks

1. Introduction

The production of solar energy is subject to strong spatial and temporal fluctuations due to the dependence on meteorological boundary conditions. This leads to uncertainties in the planning of energy supplies and, thus, to economic inefficiencies. With a reliable solar performance forecast, uncertainty is minimized while load and storage management can be optimized. Thus, prediction of solar irradiation makes an important contribution to efficient and economical applications for many areas of solar energy use, while high-quality one-minute data series are key to understanding the dynamic interaction of photovoltaic (PV) systems, loads, and grids [1].

Worldwide, the installed PV power increases by a double-digit percentage per year [2]. This trend makes photovoltaics an even more important alternative for global power supply. New models for the forecast of solar energy production can help to reduce the difficulties of integrating PV systems into existing power supply structures. In order to optimally manage the power supply, electricity producers are compelled to provide a forecast of the expected delivery quantities [3]. With the help of reliable predictive models, the market price of the solar energy is then determined by supply and demand.

Many solar applications such as PV systems and grid regulation depend critically on the ability to predict cloud movement [4,5]; therefore, sky cover information is a potentially useful input for improving the prediction accuracy of the energy feed-in of solar power systems [6].

Other techniques for predicting solar irradiation are methodologies employing the temporal evolution of all-sky images. Most prediction methodologies focus on cloud identification and motion. Alonso-Montesinos et al. [7] and Marquez and Coimbra [8] achieved this by detecting cloud motion vectors from all-sky images for forecasting short-term predictions of solar radiation. Sky coverage information provided by all-sky images has been successfully used for forecasting minutes ahead of solar irradiance. The results of this investigation showed an accuracy above 17% over the persistence model [9]. In addition, a study by Chow et al. [10] showed that the maximum possible forecast horizon with all-sky images was highly dependent on cloud speed.

Wu and Chan [11] compared a linear statistical autoregressive–moving-average (ARMA) model, a nonlinear artificial neural network (ANN) model, and a hybrid model between both, and they found that the deviation of the data in the ARMA was higher than that in the ANN. ARMA provided a better result for linear components, while the ANN showed a smaller deviation for nonlinear components. ARMA showed better predictions at very low irradiance, while the neural network performed better at high irradiance. The study by Kamadinata et al. [12] developed and compared two different simple methodologies utilizing two ANNs. The first one predicted cloud movement direction, while the second ANN predicted solar radiation using the output of the first ANN as input.

The persistence model is the most common reference model for short-term forecasting of solar irradiance [13,14]. This model supposes that the data at x_{t+1} equals the data at x_t. Generally, for solar irradiation predictions, the persistence model is unreliable for forecasting more than one hour in advance [15,16].
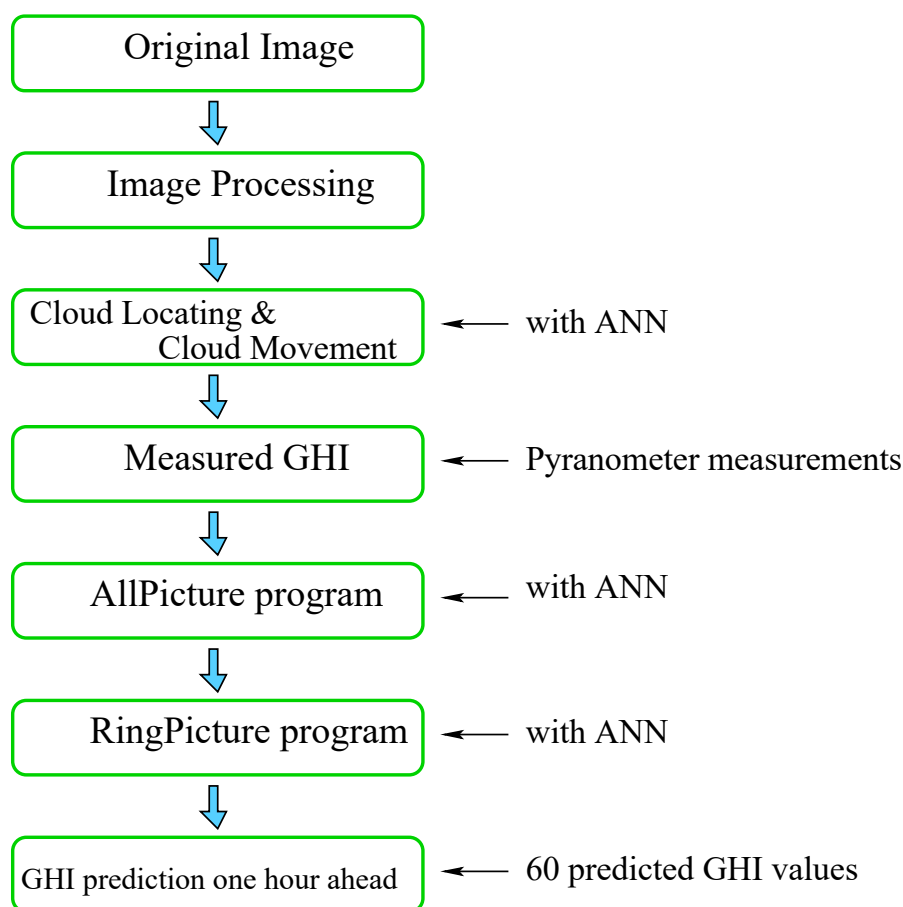
The study we present here shows that by applying our method, the solar irradiance can be estimated in one-minute resolution by simulating one hour ahead at the Institute of Meteorology and Climatology (IMuK), Leibniz Universität Hannover, Hannover, Germany. In addition, this study does not require meteorological inputs such as, e.g., humidity, wind speed, or air temperature. Therefore, in further studies the new algorithm could be applied under diverse weather conditions elsewhere.

2. Methods

We developed a new algorithm to predict future data based on observed data, i.e., time series of 60 one-minute values of the global horizontal irradiance and, as their sum, the total amount of energy one hour ahead. It was based on a four-year dataset of all-sky images and the respective thermopile pyranometer measurements that were used as input to machine learning methods.

The algorithm consisted of three main steps. The first part comprised the data preparation for an image processing program and the creation of a program to export pyranometer measurements for the input parameters (Section 2.1). Figure 1 shows the forecast process of the global horizontal irradiance (GHI) with all-sky images and an ANN.

The second part of the study was the creation of three different ANN programs. The *Cloud Locating and Cloud Movement Program* (Section 2.2), the *AllPicture Program*, and the *RingPicture Program* (Section 2.3). The third part consisted of the validation of the new model (Section 2.4). Table 1 shows the preparation and methodology of these three steps.

```
┌─────────────────────────┐
│      Original Image      │
└─────────────────────────┘
             ↓
┌─────────────────────────┐
│     Image Processing     │
└─────────────────────────┘
             ↓
┌─────────────────────────┐
│   Cloud Locating &       │ ← with ANN
│   Cloud Movement         │
└─────────────────────────┘
             ↓
┌─────────────────────────┐
│      Measured GHI        │ ← Pyranometer measurements
└─────────────────────────┘
             ↓
┌─────────────────────────┐
│    AllPicture program    │ ← with ANN
└─────────────────────────┘
             ↓
┌─────────────────────────┐
│   RingPicture program    │ ← with ANN
└─────────────────────────┘
             ↓
┌─────────────────────────┐
│ GHI prediction one hour ahead │ ← 60 predicted GHI values
└─────────────────────────┘
```

Figure 1. Process of the forecast of the global horizontal irradiance (GHI) with all-sky images and an artificial neural network (ANN).

Table 1. Summary of data preparation and methodology. Step I-selected inputs and the Cloud Movement program. Step II-two different ANNs with their respective inputs and output parameters. Step III-comparison of the neural network and the persistence model. The sun zenith angle (SZA) is the angle between the zenith and the centre of the sun's disc.

Step	Task	Input	Output
Step 1 (a)	Extraction of parameters from all-sky images as input for next steps.	• RGB channel statistics ○ Average ○ Mode ○ Median ○ Standard deviation • Sky cover (%) • Clouds in the sky (%)	
	Extraction of two extra inputs for next steps	• GHI_{Mea} • SZA	
Step 1 (b)	Cloud Locating and Cloud Movement program (works with an ANN)	• All-sky images • Current position of the clouds	Cloud position one minute ahead

Table 1. *Cont.*

Step	Task	Input	Output

Step 2 (a)	Creation of the AllPicture program (preconditioning for seasonal and diurnal variations)	For each image:
		• RGB channel statistics
		  ○ Average
		  ○ Mode
		  ○ Median
		  ○ Standard deviation
		• Sky cover (%)
		• Clouds in the sky (%)
		• GHI_{Mea}
		• SZA
		• Cloud position one minute ahead
			GHI_{Sim}

Step 2 (b)	Creation of the RingPicture program	For each ring:
		• RGB channel statistics
		  ○ Average
		  ○ Mode
		  ○ Median
		  ○ Standard deviation
		• Sky cover (%)
		• Clouds in the sky (%)
		• GHI_{Sim}
		• SZA
		• Cloud position one minute ahead
			$GHI_{SimFinal}$

Step 3	Validation	• ANN model output • Persistence model output	• 60 one-minute values • Hourly sum • Deviations

2.1. Setup of the ANN

Different numbers of neurons for the input parameters for the three ANN programs were used; see Table 2. The *Cloud Locating and Cloud Movement* program used eight inputs and one output, while the *AllPicture* and the *RingPicture* programs each used nine inputs and one output.

Finally, two hidden layers with varying numbers of neurons were necessary for each network. The number of hidden neurons in a single hidden layer was calculated by Equation (1):

$$m = \sqrt{n + l} + \alpha, \tag{1}$$

where n is the number of input parameters and l is the number of output neurons; α is a constant ranging between 1 and 10.

In an ANN, the connection between input, hidden, and output neurons was established by synaptic weights and transfer Equation (2). The input information x_j flows through connections that multiply its strength by a weight $w_{i,j}$ to reach a product $w_{i,j}x_j$. This product is the argument for a transfer function f that gives the output y_i.

$$y_i = f(\sum_{j=1}^{n} w_{i,j}x_j) \tag{2}$$

The activation function f defines the output of a neuron in terms of the induction of the linear field y_i. The activation function calculates the state of activation of a neuron, transforming the global input into a state of activation.

The Levenberg–Marquardt (LM) algorithm, a combination of the Grade and the Gauss–Newton method, was used as learning algorithm. It was used as it is less time consuming and also has the local convergence of the Gauss–Newton method and the complete properties of the Grade method [17].

Table 2. The neural network structure used to carry out this investigation.

ANN Programs	No. of Input Parameters	No. of Hidden Layers	No. of Neurons in the First Hidden Layer	No. of Neurons in the Second Hidden Layer	No. of Output Neurons
Cloud Locating and Cloud Movement program	8	2	4	2	1
AllPicture program	9	2	7	5	1
RingPicture program	9	2	7	5	1

2.2. Image Acquisitition and Data

The results of Toshing et al., 2013 [18] demonstrated the development of a camera system at IMuK, where the projection of the camera system was found to be nearly equidistant. The pictures for this study were recorded with both a Canon G10 and a Canon EOS 700D, using an exposure time of $1000/s$. The Hemispherical Sky Imager (HSI), installed on the roof of IMuK, comprises commercial compact CCD (charge-coupled device) cameras equipped with a fish-eye lens providing a $183°$ field of view. The maximum image size is 4416×3312 pixels, corresponding to 3.5 million pixels for the hemispherical image with a radius of 1060 pixels. In addition, the global irradiance was measured simultaneously using a CMP11 pyranometer (Kipp & Zonen, Delft, The Netherlands), [19].

2.3. Images Preprocessing

A software program capable of identifying the area of the sky covered by clouds was developed and used at IMuK. The work of Yamashita et al. [20] permitted the calculations of the sky index from an original picture. However, in this study we calculated the *Haze Index* (Equation (3)), as stated by Schrempf [21], to improve the cloud identification on the basis of the sky index. An example of the haze index is displayed in Figure 2c.

$$Haze\ Index = \frac{\frac{count_{red}+count_{blue}}{2} - count_{green}}{\frac{count_{red}+count_{blue}}{2} + count_{green}} \qquad (3)$$

The Sun Zenith Angle (SZA) algorithm (a free Matlab (Matlab_R2016b) code sample [22]) was extended at IMuK for this study. The output of this program was one-minute solar position values for the location at IMuK. The SZA was the most important input parameter for training the network and for delivering the output parameters in the simulation phase.

2.4. Cloud Locating and Cloud Movement Program

To obtain two new input parameters for the next steps, it was necessary to create an algorithm capable of detecting clouds and predicting their movements. A cloud detection algorithm was used to determine the percentage of clouds in the sky. This method provided automated cloud detection operating in the red and blue channels [23] using super-pixel segmentation [24].

The total sky and cloud area were calculated followed by the percentage of clouds present, i.e., with help of the Haze Index. The cloud pixels were then identified as they were needed to find the cloud locations. If cloud pixels were high, the algorithm drew a contour around the cloud area until the density decreased in the side areas. At low cloud pixels, the algorithm recognized this as a boundary of the cloud.

In our system, as the output parameter, the ANN learned to predict the position of the clouds one minute ahead by combining the movement between Figure 2d,e. The idea was to predict when the clouds would appear in front of the sun, as shown in Figure 2d. The algorithm follows the clouds from the horizon to the center of the sun, taking information from each ring.
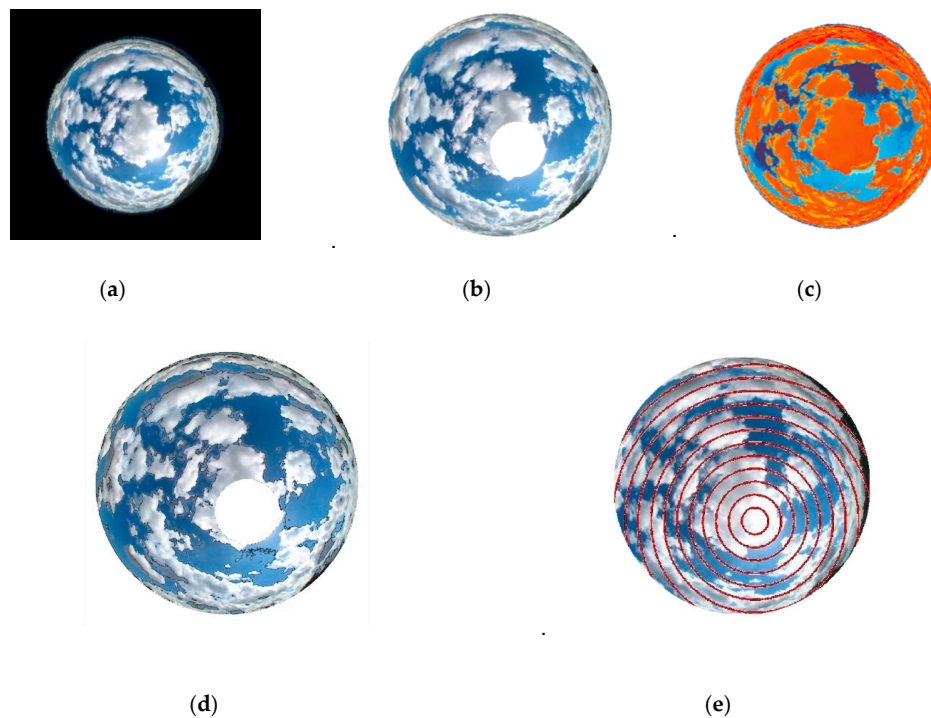
Figure 2. (**a**) Original image. (**b**) Cropped black area of the picture and coverage of the sun. (**c**) Haze Index image. (**d**) The picture from the Cloud Locating and Cloud Movement program. In addition, the black contour around the clouds show the possible clouds that could appear over the sun in the next minutes. (**e**) The picture shows the circles from the center of the sun with uniform distance to the horizon.

Accordingly, the input parameters for the Cloud Locating and Cloud Movement program were the SZA; measured global horizontal irradiance (GHI_{Mea}); current cloud position (derived from the actual image as described before); percentage of clear sky; percentage of clouds in the sky; and the mathematical average, mode, median, and standard deviation of the RGB channels. The output parameter was the cloud position for the next minute. This output parameter was introduced as an input parameter for the next ANN. The statistical information of each channel and the percentage of clear sky and cloud cover were obtained without taking into consideration the sun's circumference to avoid oversaturation of the pixels (Figure 2b). In addition, the extraction of the statistical information from the pictures was limited to the time from sunrise to sunset.

2.5. Creation and Training of the AllPicture Program and RingPicture Program

In this step, we created two new ANNs with respective training and simulation processes. A comparison between the different models in terms of training time and prediction deviation indicated that the LM algorithm was the most efficient prediction model. The selection of this learning algorithm was especially important for the training and simulation time processes. The input datasets were divided into 36 months for the training phase and 6 months for the validation.

The simulation of the AllPicture program was preconditioned with training runs on whole images. The input parameters of this ANN were SZA; GHI_{Mea}; percentage of clear sky; percentage of cloud cover; average, mode, median, and standard deviation of the RGB channels; and cloud position for the next minute. The output of this ANN was the GHI_{Sim}, and it was used as input to the next ANN, the RingPicture program. Since no time-based information was used in this algorithm, the aim of this ANN preconditioning was to allow it to learn the seasonal and diurnal variations of the solar irradiance.

The second step was the simulation of the RingPicture program, where the actual simulation of the 60 one-minute values takes place. The input parameters of this ANN were SZA; GHI_{Sim}; percentage of clear sky; percentage of cloud cover; average, mode, median, and standard deviation of the RGB

channels; and cloud position for the next minute. The training target and, hence, the most important output of the algorithm was the hourly $GHI_{SimFinal}$, calculated as the sum of the 60 one-minute values. Thus, while the AllPicture program worked over the whole picture, the RingPicture program worked over each ring of the picture, i.e., the program considered each ring as a picture (see Figure 2e).

For the simulation of the 60 one-minute values and the resulting hourly $GHI_{SimFinal}$, only one image was needed. The image was subdivided into concentric rings around the sun (Figure 2e). The rings had a temporal resolution of one minute; the width depended on the distance from the horizon due to the equidistant projection. For each ring, the same statistical information from the first step was extracted, while the SZA was also adjusted according to the progress in time that the ring represents. With these inputs and the GHI_{Sim} of the whole image from the first step of Part 2, the ANN simulated the GHI of each ring. Ring after ring was simulated subsequently, starting from the center of the sun and moving to the horizon. The number of simulated minutes, n, depended on the cloud position and the position of the sun.

After the last ring was processed, the calculation method changed in order to calculate the missing one-minute values from *n* to 60. The statistical information of the last ring was taken and searched for in the database of recorded images. The image that best matched the statistical information was selected, taking into consideration the sun position, time of year, and time of day. To simulate $GHI_{SimFinal}$ at *n* + 1, the image was processed. This process was repeated until all 60 values had been generated.

The total $GHI_{SimFinal}$ for one hour was calculated as the sum of the 60 one-minute values and compared to the measured GHI_{Mea} value. The deviation was fed back to the ANN until the deviation reached a defined minimum threshold.

2.6. Validation of the New Model

The persistence model assumes that the global irradiation data at x_t is similar to the global irradiation data at x_{t-24h}, This model was very useful for benchmarking other methods [25]. We assumed that an average of seven days was sufficient to predict the irradiance with the persistence model. When considering only one day, the persistence model would be influenced too much by the current variability. When considering more than seven days, the simulation did not improve any further.

Figure 3 shows the persistence model's forecast for two days in more detail. This model processed the information to the end time of the desired simulation. On the day of the simulation, the persistence model processed the information just until the simulation began, thus delivering the simulated hour.

(a)
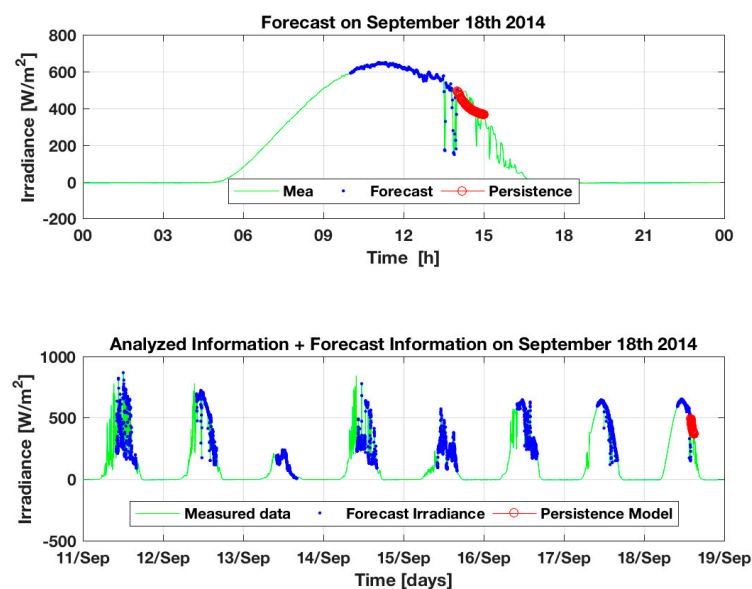
Figure 3. *Cont.*
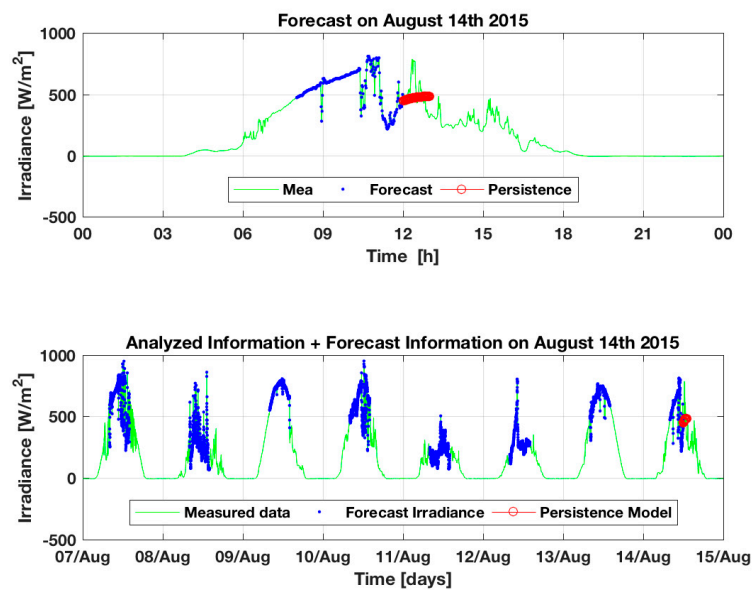
Figure 3. Prediction from the reference persistence model for two different days: (**a**) 18 September 2014 from 14:01 to 15:00. (**b**) 14 August 2015 from 12:01 to 13:00. The red dots on the lower part of both images indicate the simulated time. The blue dots indicate that the data employed for the simulation was one hour previous to this from the last seven days. The upper part shows a zoom of the simulation day.

3. Results

The following days were selected for validating the new algorithm: 18 September 2014; and 10 January, 14 August and 21 August, 2015. The selected days represented different weather conditions with high solar irradiance variability. The root-mean-square error (RMSE) (Equation (4)), mean absolute error (MAE) (Equation (5)), and the coefficient of determination (R^2) (Equation (6)) were used to evaluate the performance of the new model for these four days. In addition, 17 July 2015 was selected to simulate 13 h from 05:01 to 18:00. Definitions are expressed as follows:

$$\text{RMSE} = \sqrt{\sum_{i=1}^{N} \frac{\|y_i - x_i\|}{N}}, \tag{4}$$

$$\text{MAE} = \frac{\sum_{i=1}^{N} |y_i - x_i|}{N}, \tag{5}$$

$$R^2 = \sum_{i=1}^{N}(y_i - \overline{y})(x_i - \overline{x}) / \left[\left(\sum_{i=1}^{N}(y_i - \overline{y})^2 \right) \left(\sum_{i=1}^{N}(x_i - \overline{x})^2 \right) \right]^{1/2}, \tag{6}$$

where y_i is the forecast value, x_i is the measured value, and N is the number of samples. Additionally, $\overline{x} = \sum_{i=1}^{N} x_i$ and $\overline{y} = \sum_{i=1}^{N} y_i$. Finally, to validate our model, i.e., for knowing how many simulations we had to carry out for the validation of the new model, statistical sampling (Equation (7)) was utilized, and the results are presented as a boxplot. The definition of the statistical sampling is expressed as follows:

$$x = \left(Z^2 N p q \right) / \left(e^2 (N-1) Z^2 p q \right), \tag{7}$$

where N is the total of the set, $p = 0.95$, $q = 0.05$, and $Z = 1.96$ (this value corresponds to the confidence level of 95%).

3.1. Analysis of One-Hour-Ahead Results

Figure 4 shows the forecasts of one-hour-ahead simulation for four days using the new algorithm and the persistence model. These values were compared with the measured data. The results show that the forecast values of the ANN model closely matched the measured values, and both the RMSE and the MAE were smaller in the new ANN model than in the persistence model for the entire simulated hour (see Tables 3 and 4).
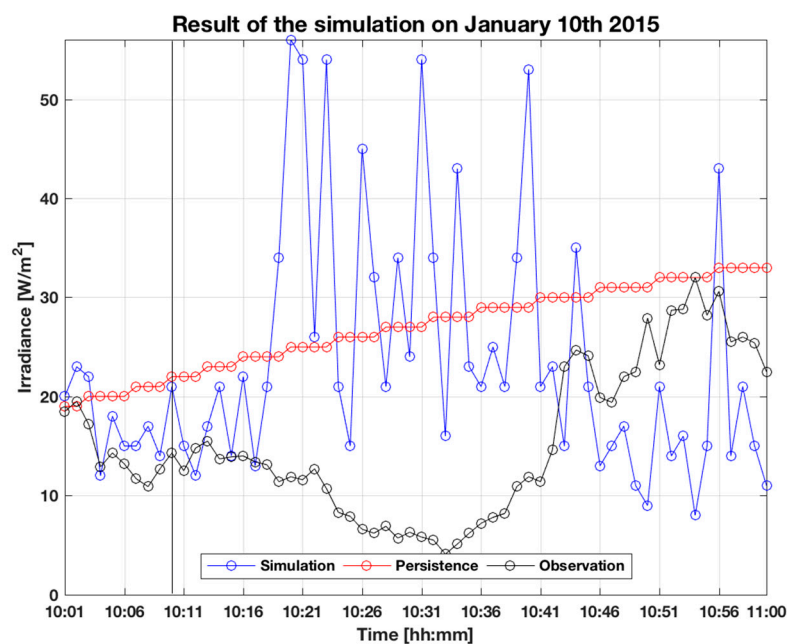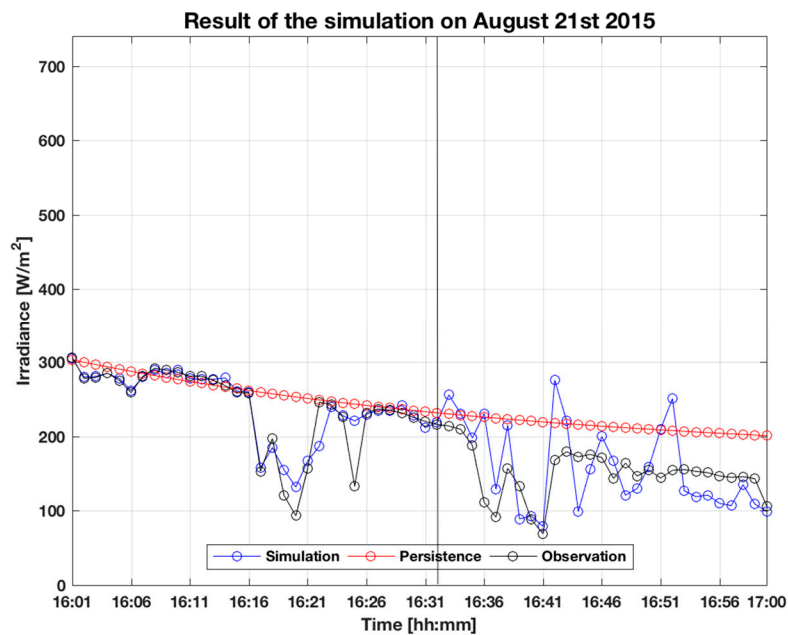

(**a**)

(**b**)

Figure 4. *Cont.*

(**c**)

(**d**)
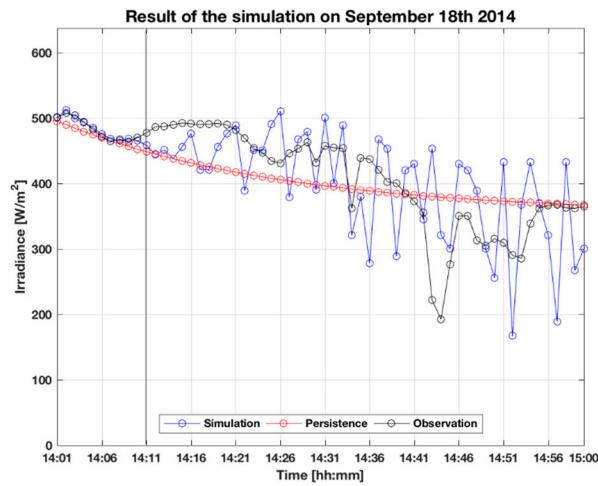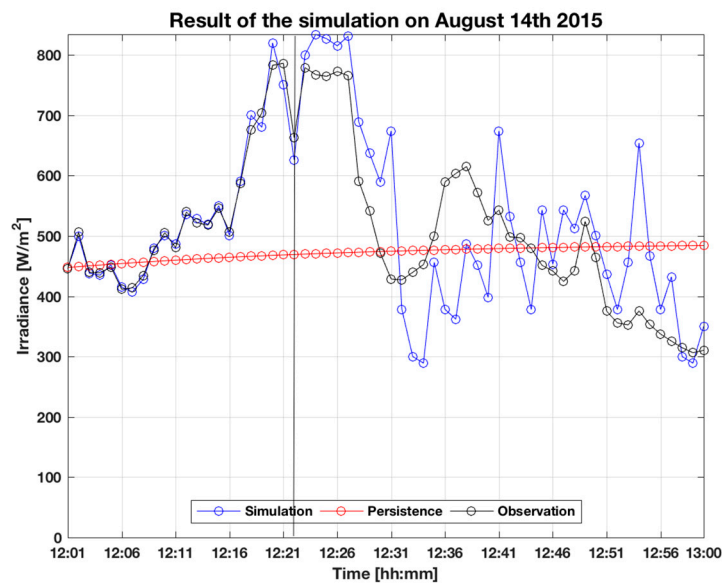
Figure 4. Comparison of new ANN model and persistence model for one-hour-ahead simulation. The vertical black lines in the graphs represent the border of minutes of future information from the last taken picture. (**a**) shows a good prediction of the total amount of energy with R^2 = 0.92. (**b**) shows a good prediction especially for the first minutes of simulation. (**c**) shows a good prediction for the first 32 min of simulation. (**d**) shows a very important deviation with respect to the measured data; R^2 = 38. However, irradiance values of under 80 W/m^2 are of minor importance for the overall energy forecast.

The new algorithm was able to produce forecasts of higher quality compared to the reference persistence model, even when it stopped receiving information from the last picture. The last pictures were taken at 14:00 on 18 September 2014, at 12:00 on 14 August 2015, at 16:00 on 21 August 2015

and at 10:00 on 10 January 2015 and provided the algorithm with 11, 22, 32, and 10 min of future information, respectively. The most important improvement was the decrease in RMSE and MAE of the total energy received at the surface over one hour. Figure 4d shows a particular simulation case where the measured irradiance was very low—between 4 W/m^2 and 32 W/m^2. Under low irradiance conditions, the network did not predict adequately when it stopped receiving information from the last taken picture; see Table 3. The measured irradiation value at IMuK on 10 January, 2015 was 15 Wh/m^2 between 10:01 and 11:00. Our model simulated a total of 24 Wh/m^2, i.e., a difference of 9 Wh/m^2 (54%). In comparison, the persistence model predicted a total of 27 Wh/m^2, a difference of 12 Wh/m^2, which corresponds to 76%. The new model does not significantly outperform the persistence model. For very small irradiance levels, the ANN does not have the same effectiveness as for high irradiance levels. However, forecasts with very low irradiance levels were of minor relevance for solar energy forecasts. On September 18, 2014, from 16:01 to 17:00, the irradiation measured at IMuK was 414.8 Wh/m^2 and the new model simulated 412.3 Wh/m^2, which corresponds to a difference of 2.5 Wh/m^2 (0.06%). The persistence model predicted 408.3 Wh/m^2 with a difference of 6.5 Wh/m^2, corresponding to 1.6% (Tables 3 and 4).

Table 3. Comparison of the statistical indicators of the new ANN forecast model against the persistence forecast model on four different days. The table compares the information until the last picture with the information after the last picture.

Simulation Day	Models to Compare	With Information from the Last Picture				When the Last Picture Does Not Provide Information Anymore			
Day	Model	Minutes	RMSE (Wh/m^2)	R^2	MAE (Wh/m^2)	Minutes	RMSE (Wh/m^2)	R^2	MAE (Wh/m^2)
18 Sepetember 2014	ANN	11	7	0.92	5	49	77	0.52	61
	Persist		14	0.85	12		69	0.38	98
14 August 2015	ANN	22	12	0.99	8	38	111	0.77	90
	Persist		111	0.77	74		149	0.13	116
21 August 2015	ANN	32	21	0.92	10	28	49	0.55	39
	Persist		51	0.58	29		72	0.17	65
10 Jane 2015	ANN	10	4	0.78	3	50	20	0.42	16
	Persist		7	0.71	6		14	0.64	13

Table 4. Summary of the statistical indicators of the new ANN forecast model for four different days.

Day	Hour	Total Measured Energy (Wh/m^2)	Total Simulated Energy (Wh/m^2)	Difference (Wh/m^2)	RMSE (Wh/m^2)	R^2	MAE (Wh/m^2)
18 September 2014	14:01–15:00	414.8	412.3	2.5	69	0.61	50
14 August 2015	12:01–13:00	510	521	11	91	0.79	62
21 August 2015	16:01–17:00	197	203	6	37	0.84	24
10 January 2015	10:01–11:00	15	24	9	19	0.38	14

3.2. Analysis of the Daily Integrated Irradiation

The hourly average of the simulation for one day on 17 July 2015 from 05:01 to 18:00 is shown in Figure 5. When making a prediction for an entire day, it was necessary to take a picture every 60 min.
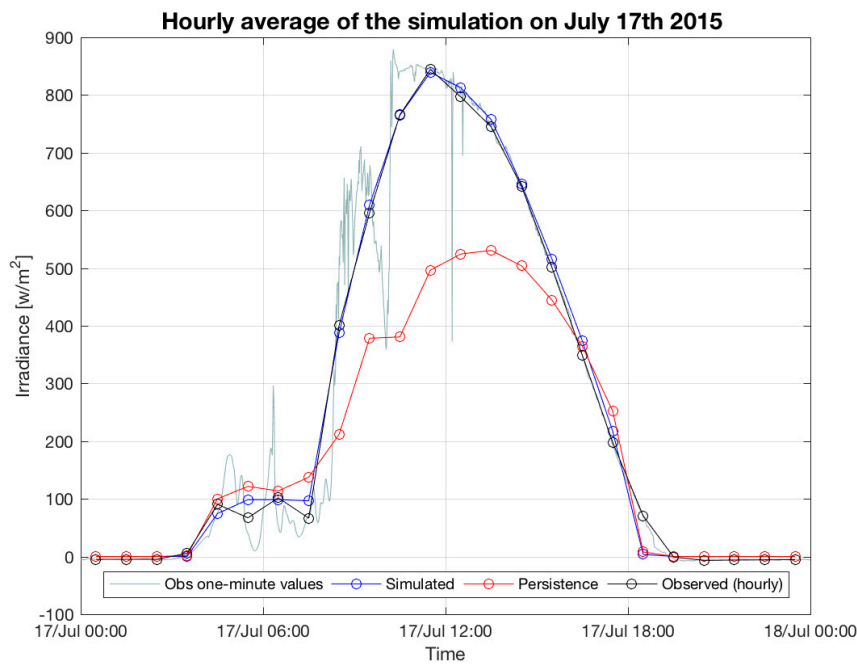
Figure 5. The hourly average of simulation on 17 July 2015 from 05:01 to 18:00. The grey line shows the measured one-minute values.

In Figure 5 we see that the persistence model, as a linear statistical model, cannot describe the performance for days with broken clouds as accurately as the new ANN model can. Table 5 compares the statistical indicators of the global irradiance for the one-hour prediction on 17 July 2015 from 05:01 to 18:00 using the new ANN model and the persistence model.

Table 5. Comparison of the statistical indicators of the ANN forecast model against the persistence forecast model on 17 July 2015 at 05:01 to 18:00.

Model	RMSE (Wh/m^2)	R^2	MAE (Wh/m^2)
ANN	65	0.98	30
Persistence	91	0.91	63

3.3. Analysis of the Statistical Sampling

Figure 6 shows the distribution of the relative deviations as boxplots. The results of Figure 6a suggest that the new model shows a symmetrical approach for 50% of the sample rate for the first several simulation minutes. Nevertheless, Figure 6b shows an asymmetrical distribution of outliers and a decreasing number of outliers for higher sample sizes, leading to higher uncertainties in the simulation of the data. As expected, the uncertainty of the new model decreased as soon as more simulation data were introduced and remained constant with the increase of sample sizes. It is worth noting that in the persistence model, the uncertainty increased as soon as more simulation data were introduced.

(**a**)

(**b**)
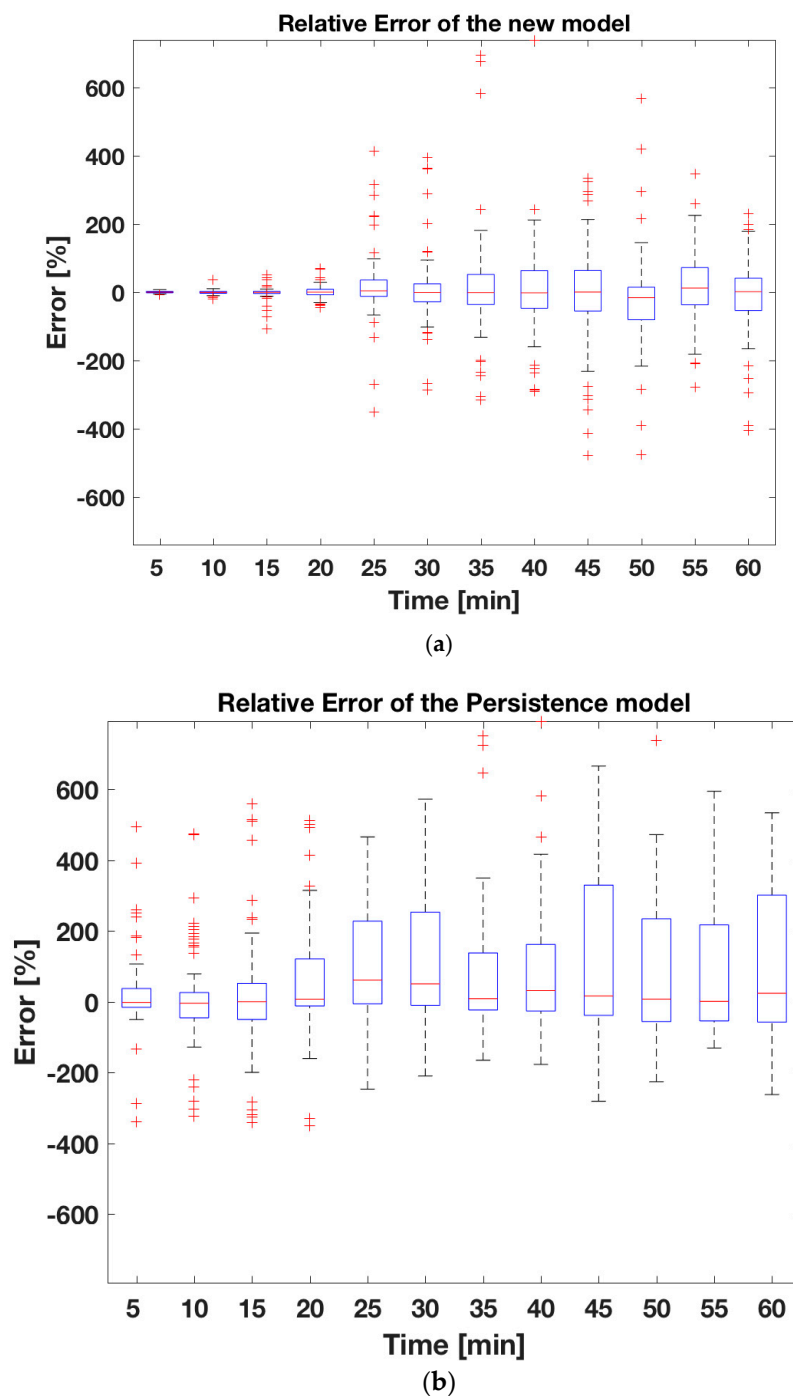
Figure 6. The relative deviation boxplot of the simulation derived for different time horizons. The symmetry in 50% of the data decreases as soon as the program receives information from the last picture and increases when the program does not receive information from the last picture. (**a**) corresponds to the new ANN. Here, there are narrower interquartile ranges for higher sample sizes, but the numbers of outliers (+) are lower than in (**b**). (**b**) corresponds to the persistence model. Of the data, 50% is not exactly located in the middle, and the 25% and 75% levels of the data deviation are higher than in (**a**).

In order to estimate how many simulations were needed to carry out the validation of our model, statistical sampling was performed. Over 6 months of validation periods and assuming that we could simulate an average of 8 h every day, we got 1440 valid cases. In these 6 months, 80 cases were not considered because the irradiance level was under 100 W/m^2. Hence, our final valid cases numbered

1360 and, to validate our algorithm, we applied statistical sampling. Thus, taking into consideration a confidence level of 95% with a margin of error of 6%, our simulated cases numbered 288 (i.e., 288 h). Therefore, each interval time corresponded to one hour of simulation, and from these 288 cases, 96 cases corresponded to cloudless hours, 96 cases to overcast hours, and 96 cases to broken cloud hours. For the new method, if on the horizon the presence of clouds is zero, it is very likely that in the next few minutes, near the sun, there will be no cloud, as well. Thus, for clear sky days, the deviations varied 8% compared to the measurement values. Overcast days and days with broken clouds represented a very important challenge for the neural network. The deviations varied approximately 24% according to the type of clouds and the amount of clouds on the horizon compared to the measurement values. In addition, on days with broken clouds, the deviations varied 32% according to the percentage of clouds and blue sky between the horizon and the center of the sun compared to the measurement values. Applying the new ANN model to the 288 cases, our model achieved an average 22% deviation compared to the measurement values for all sky conditions. In contrast, the persistence model shows a 52% deviation for the three cases.

4. Conclusions

A new method developed to forecast solar irradiance one hour ahead has been presented. This new model combines the advantages of using all-sky images and an LM-ANN. The GHI predicted by the proposed methodology improves the forecast for the total amount of energy one hour ahead by reducing both the RMSE and MAE of the simulation by approximately 40% when compared to the persistence model. Furthermore, we showed here that the new model is capable of reproducing the nonlinear nature of the solar irradiance more reliably than statistical linear models.

According to the simulation results, for the first minutes of simulation, the new algorithm outperforms the persistence model. For irradiation levels under 80–100 W/m^2, the new algorithm does not accurately predict one hour ahead. However, such low irradiances are usually not relevant for the production of solar energy. Nevertheless, for higher irradiance the new algorithm can predict one hour ahead under diverse weather conditions with an average deviation of 22% within the next hour.

The model presented here has only been tested at IMuK. The neural network may be trained with datasets from other places. To achieve this, only the pictures of the desired place with the respective pyranometer measurements are sufficient. This work could be especially relevant for implementing strategies in decisions for the balance of supply and demand of electricity. Additionally, this study will be of interest for energy markets concerned with mitigating utility cost by acquiring more accurate weather predictions. It may also be important for the estimation of power output and to avoid damage to the electrical grid.

Author Contributions: Conceptualization, C.C., G.S.; Methodology, C.C., G.S; Software, C.C.; Validation, C.C., G.S. and M.H.; Formal Analysis, C.C., G.S; Investigation, C.C.; Resources, C.C. and G.S.; Data Curation, C.C.; Writing-Original Draft Preparation, C.C., G.S., and R.M.; Writing-Review & Editing, C.C., G.S., M.H., and R.M.; Visualization, C.C., R.M. and M.H.; Supervision, C.C., G.S.; Project Administration, C.C., G.S.; Funding Acquisition, C.C., G.S.

References

1. Hofmann, M.; Riechelmann, S.; Crisosto, C.; Mubarak, R.; Seckmeyer, G. Improved synthesis of global irradiance with one-minute resolution for PV system simulations. *Int. J. Photoenergy* **2014**. [CrossRef]
2. Statistiken. 2007. Available online: https://www.volker-quaschning.de/datserv/pv-welt/index.php (accessed on 9 February 2018).
3. Bundesnetzagentur (2013). Available online: https://www.bundesnetzagentur.de/DE/Sachgebiete/ElektrizitaetundGas/Unternehmen_Institutionen/ErneuerbareEnergien/ZahlenDatenInformationen/zahlenunddaten-node.html (accessed on 17 February 2018).
4. Mathiesen, P.; Kleissl, J. Evaluation of numerical weather prediction for intra-day solar forecasting in the continental United States. *Sol. Energy* **2011**, *85*, 967–977. [CrossRef]
5. Martínez, L.M.; Vargas, M.; Rubio, F.R. *Vision-Based System for the Safe Operation of a Solar Power Tower Plant*; Springer: Berlin, Germany, 2002.
6. Zhen, Z.; Wang, Z.; Wang, F.; Mi, Z.; Li, K. Research on a cloud image forecasting approach for solar power forecasting. *Energy Procedia* **2017**, *142*, 362–368. [CrossRef]
7. Alonso, M.J.; Batlles, F.J.; Portillo, C. Solar irradiance forecasting at one-minute intervals for different sky conditions using sky camera images. *Energy Convers. Manag.* **2015**, *105*, 1166–1177. [CrossRef]
8. Marquez, R.; Coimbra, C.F.M. Intra-hour DNI forecasting based on cloud tracking image analysis. *Sol. Energy* **2013**, *91*, 327–336. [CrossRef]
9. Chu, Y.; Pedro, H.T.C.; Nonnenmacher, L.; Inman, R.H.; Liao, Z.; Coimbra, C.F.M. A Smart image-based cloud detection system for intrahour solar irradiance forecasts. *J. Atmos. Ocean. Technol.* **2014**, *31*, 1995–2007. [CrossRef]
10. Chi, W.C.; Bryan, U.; Matthew, L.; Anthony, D.; Jan, K.; Janet, S.; Byron, W. Intra-hour forecasting with a total sky imager at the uc san diego solar energy testbed. *Sol. Energy* **2011**, *85*, 2881–2893.
11. Wu, J.; Keong, C.C. Prediction of hourly solar radiation using a novel hybrid model of arma and tdnn. *Sol. Energy* **2011**, *85*, 808–817.
12. Kamadinata, J.O.; Tan, L.K.; Tohru, S. Global Solar Radiation Prediction Methodology using Artificial Neural Networks for Photovoltaic Power Generation Systems. *Smartgreens* **2017**. [CrossRef]
13. Almeida, M.P.; Perpinán, O.; Navarrete, L. PV power forecast using a nonparametric PV model. *Sol. Energy* **2015**, *115*, 354–368. [CrossRef]
14. Wilks, D.S. *Statistical Methods in the Atmospheric Sciences*; Academic Press: Cambridge, MA, USA, 2011.
15. Richard, P.; Sergey, K.; James, S.; Karl, H.J.; David, R.; Thomas, E.H. Validation of short and medium term operational solar radiation forecasts in the US. *Sol. Energy* **2010**, *84*, 2161–2172.
16. Mellit, A.; Kalogirou, S.A. Artificial intelligence techniques for photovoltaic applications: A review. *Prog. Energy Combust. Sci.* **2008**, *34*, 547–632. [CrossRef]
17. Yang, H.Y.; Ye, H.; Wang, G.Z. Applications of chaos theory to load forecasting in power system. *Relay* **2005**, *33*, 26–30.
18. Tohsing, K.; Schrempf, M.; Riechelmann, S.; Schilke, H.; Seckmeyer, G. Measuring high-resolution sky luminance distributions with a CCD camera. *Appl. Opt.* **2013**, *52*, 1564–1573. [CrossRef] [PubMed]
19. Anon. Available online: http://www.kippzonen.com/Product/13/CMP11-Pyranometer#.WXi1sK3qh-U (accessed on 23 May 2018).
20. Yamashita, M.; Yoshimura, M.; Nakashizuka, T. Cloud Cover Estimation using Multitemporal Hemisphere Imageries. *Inter. Arch. Photogramm. Remote Sens. Spat. Inf. Sci.* **2004**, *35*, 826–829.
21. Schrempf, M. Entwicklung eines Algorithmus zur Wolkenerkennung in Digitalbildern des Himmels. Master's Thesis, Institut für Meteorologie und Klimatologie, Hanover, Germany, 2012.
22. Estimation, F. Full Vectorization of Solar Azimuth and Elevation Estimation-File Exchange-MATLAB Central. Available online: https://de.mathworks.com/matlabcentral/fileexchange/48594-full-vectorization-of-solarazimuth-and-elevation-estimation (accessed on 21 July 2015).
23. Yang, J.; Lu, W.; Ma, Y.; Yao, W. An automated cirrus cloud detection method for a ground-based cloud image. *J. Atmos. Ocean. Technol.* **2012**, *29*, 527–537. [CrossRef]

24. Liu, S.; Zhang, L.; Zhang, Z.; Wang, C.; Xiao, B. Automatic cloud detection for all-sky images using superpixel segmentation. *IEEE Geosci. Remote Sens. Lett.* **2015**, *12*, 354–358.

25. Hadja, M.D.; Philippe, L.; Mathieu, D. Solar irradiation forecasting: State-of-the-art and proposition for future developments for small-scale insular grids. In Proceedings of the WREF 2012-World Renewable Energy Forum, Denver, CO, USA, 13–17 May 2012; pp. 1–8.

4.3 Convolutional Neural Network for High-Resolution Cloud Prediction from Hemispheric Sky Images

4.3.1 Declaration of contributions

I and Gunther Seckmeyer conceived the idea to accurately determine from all-sky images the changes of the cloud shape one minute ahead using convolutional neural networks. Eduardo Luiz provided the data together we analyzed the data. I programmed all programs and created all visualizations. All authors contributed substantially with comments and revised the manuscript.

4.3.2 Published article

Cristian Crisosto, Eduardo W. Luiz, Gunther Seckmeyer.:, Convolutional Neural Network for High-Resolution Cloud Motion Prediction from Hemispheric Sky Images. *Energies 2021, 14, 753.*

Convolutional Neural Network for High-Resolution Cloud Motion Prediction from Hemispheric Sky Images

Cristian Crisosto *, Eduardo W. Luiz [ID] and Gunther Seckmeyer [ID]

Institute for Meteorology and Climatology, Leibniz Universität Hannover, Herrenhäuser Straße 2, 30419 Hannover, Germany; luiz@muk.uni-hannover.de (E.W.L.); seckmeyer@muk.uni-hannover.de (G.S.)
* Correspondence: crcrisos@gmail.com or crisostogonzalez.cristian@mh-hannover.de; Tel.: +49-511-762-4453

Abstract: A novel high-resolution method for forecasting cloud motion from all-sky images using deep learning is presented. A convolutional neural network (CNN) was created and trained with more than two years of all-sky images, recorded by a hemispheric sky imager (HSI) at the Institute of Meteorology and Climatology (IMUK) of the Leibniz Universität Hannover, Hannover, Germany. Using the haze indexpostprocessing algorithm, cloud characteristics were found, and the deformation vector of each cloud was performed and used as ground truth. The CNN training process was built to predict cloud motion up to 10 min ahead, in a sequence of HSI images, tracking clouds frame by frame. The first two simulated minutes show a strong similarity between simulated and measured cloud motion, which allows photovoltaic (PV) companies to make accurate horizon time predictions and better marketing decisions for primary and secondary control reserves. This cloud motion algorithm principally targets global irradiance predictions as an application for electrical engineering and in PV output predictions. Comparisons between the results of the predicted region of interest of a cloud by the proposed method and real cloud position show a mean Sørensen–Dice similarity coefficient (*SD*) of 94 ± 2.6% (mean ± standard deviation) for the first minute, outperforming the persistence model (89 ± 3.8%). As the forecast time window increased the index decreased to 44.4 ± 12.3% for the CNN and 37.8 ± 16.4% for the persistence model for 10 min ahead forecast. In addition, up to 10 min global horizontal irradiance was also derived using a feed-forward artificial neural network technique for each CNN forecasted image. Therefore, the new algorithm presented here increases the *SD* approximately 15% compared to the reference persistence model.

Keywords: all-sky image; cloud motion prediction; convolutional neural network

1. Introduction

Short-time cloud motion prediction has a huge impact on the future behavior of the power generation output of solar photovoltaic (PV) power plants [1]. Clouds are a major modulator of the global horizontal irradiance (GHI) and a source of severe fluctuation when, for example, passing in front of the sun. Clouds can even increase the solar radiation at the surface by reflection and/or forward scattering [2–4]. To compensate for these ramp events, very short-term forecasting/forecasts can help power plant operators to accurately manage PV power plants. The analyses of clouds play an important role in both scientific and business enterprises, where these severe fluctuations in the energy output are incompatible with the established safety standards for the electricity distribution systems [5].

In this context, the introduction of hemispheric sky imager (HSI) systems as efficient ground surface equipment for cloud data assessment have already been proven by various authors [6]. However, even with good high-resolution cloud detections, cloud movement forecast is still a topic of research due to its high degree of complexity [7–9]. Figure 1 shows how quickly cloud changes can occur within three minutes.

(a)   (b)   (c)
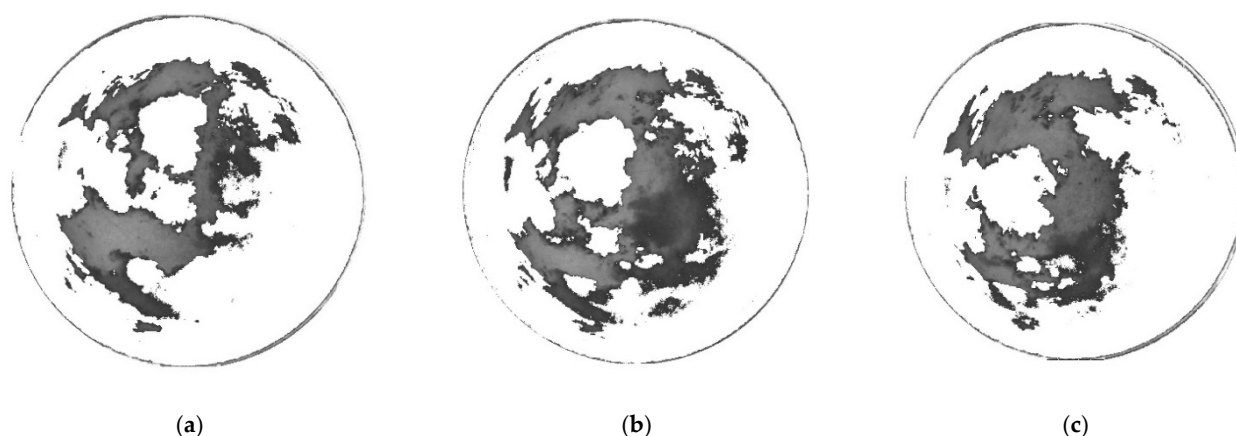
Figure 1. From (**a**–**c**); hemispheric sky imager (HSI) images showing examples of cloud shape changes within a 3-min interval. The gray area corresponds to sky pixels and white area corresponds to clouds. All cloud identification was derived from the original HSI pictures.

Looking at cloud detection methods, we can mention threshold-based algorithm [10] and machine learning methods [11–15]. Threshold-based algorithms normally use a red/blue ratio of the three RGB (red, blue, and green) channels from the image pixels for cloud classification [16–19]. Cloud pixels are identified as high R and B values, while sky pixels have low R and high B values. However, this method has some weaknesses, primarily distinguishing or detecting clouds near the horizon and close to the sun [20]. In addition, different pattern recognition algorithms have been developed. Ren and Malek [21] proposed a cloud segmentation algorithm utilizing superpixel. This algorithm divides the image into blocks (or clusters) and the division is based mainly in the continuity of cloud contours, the texture and brightness of each pixel. A hybrid framework has been proposed to forecast hourly global solar radiation [22]. This approach includes two different methods: support vector machine and machine learning techniques. The results showed that it is possible to predict next-day hourly values of solar radiation by reducing the root mean absolute error ($rMAE$) by 15.2% compared to the reference persistence model.

Machine learning methods have been used successfully for cloud detection [23] and cloud coverage estimations [24]. Crisosto [25] developed a method using HSI images to predict cloud concentrations one minute in advance using artificial neural networks (ANNs). The results showed a 30% reduction of errors when compared to the persistence model under diverse cloud conditions. In addition, a similar method has been used as an important step for predicting GHI one hour in advance with one-minute intervals [26]. Other advanced and sophisticated techniques, like convolutional neural networks (CNNs), have been developed and applied in recent years to forecast solar irradiance [27] by offering significant advantages for large image datasets [28], evaluating the non-linearity and other more complex relationships [29].

The main objective of this work is to propose a preliminary pre-processing method required to target solar irradiance predictions that allows companies to make more accurate horizon time predictions. The CNN algorithm can be important for very short-term GHI forecasts, and subsequently better marketing decisions for primary and secondary control reserve (cloud position and the GHI up to 5 min in advance). In this paper, deformation cloud vectors 10 min ahead were determined under different cloud and all-weather conditions. We applied an ANN technique to estimate the respective GHI of the forecasted cloud clusters, for methodology validation. Section 2 briefly describes the data acquisition methods. The methodologies of this study are described in Section 3. The results are given in Section 4. The conclusions and future work are discussed in Section 5.

2. Data

The HSI equipment used was a digital compact charge-coupled device camera and a fish-eye objective with a field of view of 183° inside a weatherproof box, which provided hemispherical images of the entire sky [30]. Exposure time was 1000/s, and there was an acquisition time of 1 min between each image. In total, 150,000 pictures were produced between 2014 and 2016. From these 150,000 manually segmented images, 5000 were selected for testing (i.e., these pictures were independent of the training data). The system is installed on the roof of the Institute of Meteorology and Climatology (IMUK) of the Leibniz University Hannover in Germany (52.4° N, 9.7° E). Completely overcast images were not used in this analysis, since GHI values under 100 W/m^2 are usually not relevant for the production of solar energy and we were more interested in larger GHI ramp effects. In addition, the GHI data was obtained using a CMP11 pyranometer (Kipp & Zonen, Delft, The Netherlands) [31].

3. Methodology

3.1. Cloud Identification

The method used to identify and separate clouds and sky pixels is an improved sky index image-processing algorithm [32]. The haze index consists of identifying cloud pixels combining the red, blue, and green channels, as detailed by Schrempf [33], and serves as an improvement for hazed areas. Every pixel is then classified as cloudy or clear sky based on a threshold (see Figure 3). Equation (1) presents the haze index, which is applied only to hazed areas, based on thresholds of the sky index.

$$Haze\ Index = \frac{\frac{count_{red} + count_{blue}}{2} - count_{green}}{\frac{count_{red} + count_{blue}}{2} + count_{green}} \tag{1}$$

3.2. Semantic Segmentation (Acquiring Labelled Data)

Deep learning and specifically CNNs have drastically improved the way in which intelligent algorithms learn. With convolutional layers, pooling layers, and fully connected layers, CNNs allow computational models to represent data with multiple levels of abstraction [34]. With the automatic cloud–sky separation derived by the haze index algorithm, the automatic cloud segmentation is realized. Therefore, cloud clusters are labelled as ground truth for the automatic segmentation, and thus, for further cloud motion forecasts. Sky clusters were not taken into consideration. Figure 2 shows the process of acquiring the ground truth for the input parameters of the CNN. The first column shows the original image. The results of the haze index algorithm can be seen in the second column. The third column shows the two classes: cloud clusters in white and sky clusters in gray. We can see how the CNN learns to recognize different regions of interest (ROIs) for further simulations. The training process consists of learning how clouds can change frame by frame consecutively.
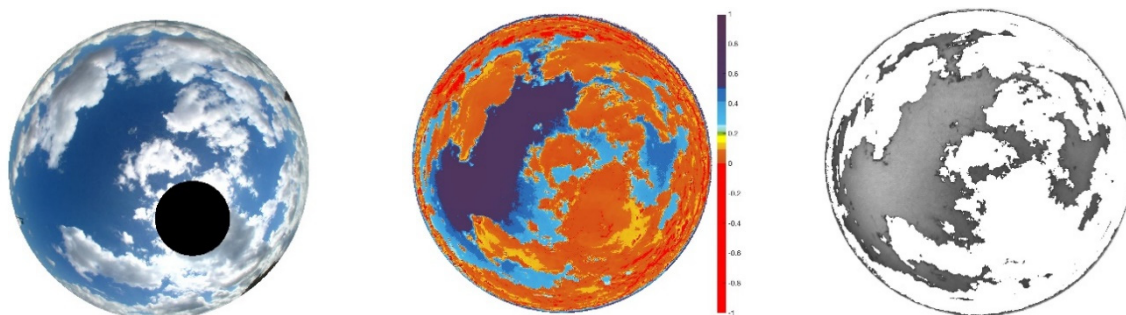
Figure 2. Automatic segmentation of a picture taken on 22 June 2014 at 12:53. The first column shows the original image. The results of the haze index algorithm can be seen in the second column. The third column shows the two classes: cloud clusters in white and sky clusters in gray.

3.3. CNN Development and Training

Once the ROIs were identified by the haze index, they were used as ground truth parameters for training the CNN. The input parameters were the original HIS images and their corresponding cloud clusters (see Figure 2). The network accepts one HIS image (.jpg) and one cloud cluster image (.jpg) and learns exactly, frame by frame, where the clouds are.

The input layers were resized to 256×256, max pooling of 2×2 resulting in an output layer of 256×256. In the training phase, a pre-trained CNN for classification and detection (VGG-16) [34] was selected and extended to automatically learn the ROI changes in whole pictures frame by frame. The training process finished when the network learned as accurately as possible the ROI changes in that time. The binary cross entropy function was minimized during the training process, and the activation layers were very simple rectified linear units, or ReLUs, defined as $ReLU(z) = max(0, z)$ or variants of this function proposed by He et al. [35]. Adaptive moment estimation (Adam) [36] was chosen as a stochastic optimization method and the batch size was 16. We trained the model using 100 epochs.

Once the trained network was ready (the network learned the cloud movements frame by frame in more than 145,000 images), the simulation phase began. The program first identified the location of the current ROI at t, and after saving this information, went back 5 min ($t - 5\Delta t$). Then the program went forward, frame by frame, to forecast the new ROI at $t + \Delta t$ by applying probabilistic accuracies learned in the training phase. In other words, the trained network delivers frame by frame the best matching cloud location, and the output is the new (estimated) ROI (cloud location) for the next minute. Furthermore, the ROI estimated for $t + \Delta t$ will be the base ROI for $t + 2\Delta t$, and so on.

3.4. An Artificial Neural Network Used for Validating Our Model

To validate the results of our algorithm, we applied an extra artificial neural network (ANN), as explained by Crisosto et al. [26]. This ANN only needs an HSI image to predict GHI one hour ahead in one-minute resolution. This input image is the output of our CNN method. Therefore, the new predicted ROIs of our algorithm were fed into the ANN as input parameters to derive their correspondent GHI values 10 min ahead.

3.5. Statistical Metrics

The Sørensen–Dice (SD) similarity coefficient [37] and overlap (VO) [38] were used for the method evaluation. SD is defined as the division between twice the number of elements common to both sets and the sum of the number of elements in each set (Equation (2)). VO is defined as a quotient of the intersection of both X and Y segmentations (Equation (3))

$$SD(X,Y) = \frac{2|X \cap Y|}{|X| + |Y|} \tag{2}$$

$$VO(X,Y) = \frac{|X \cap Y|}{|X \cup Y|} \tag{3}$$

where $|X|$ and $|Y|$ is the cardinality of two sets. The mathematical definition of the root mean square error (*RMSE*) and the coefficient of determination (R^2) are expressed as follows:

$$RMSE = \sqrt{\frac{1}{N} \sum_{i=1}^{n} (y_i - x_i)2} \tag{4}$$

$$R^2 = \left(\sum_{i=1}^{N} (y_i - \overline{y})(x_i - \overline{x}) \right) / \left[\left(\sum_{i=1}^{N} (y_i - \overline{y})^2 \right) \left(\sum_{i=1}^{N} (x_i - \overline{x})^2 \right) \right]^{1/2} \tag{5}$$

where y_i is the forecast value, x_i is the measured value, and N is the total number of samples. Additionally, $\overline{x} = \sum_{i=1}^{N} x_i$ and $\overline{y} = \sum_{i=1}^{N} y_i$.

The new algorithm was compared with the scaled persistence model [39] defined as the ROI configuration vector (*ROI_CV*) where the next minute would be identical to the current minute ($ROI\_CV_{t+1} = ROI\_CV_t$). This model is the reference model for short-term solar forecasting [40]. For the irradiance evaluation, only the movement of the sun was taken into consideration.

4. Results

For a better visual representation of the results, the following example cases were selected to show the effectiveness and efficiency of the algorithm: 15 April 2014 at 15:54, 11 July 2014 at 13:09, and 1 June 2014 at 17:42. After that, 5000 cloud images with different cloud positions were simulated and the results are presented.

4.1. Analysis of the Example Cases

Figure 3 shows the one-minute ahead simulation for the three days, including the observed (target) ROI to be simulated (column 1), the simulated ROI by our model (column 2), and the simulated ROI using the persistence model (column 3). In all cases, we can see that our CNN model performs better than the persistence for the first minute. The *SD* values were 92.4 ± 2.9% (mean ± standard deviation), 92.7 ± 2.6%, and 88 ± 3.4%, respective to each case, while the *SD* for the persistence was 85.8 ± 4.9%, 85.8 ± 5.6%, and 84 ± 7.1%, respectively.

The statistical comparison with forecasts up to 10 min ahead can be seen in Table 1. As expected, the performance of the algorithm decreases substantially as the simulated time progresses. In addition, our model outperforms the persistence model for the full 10-min period. For larger timescale forecasts (for example, 5 and 10 min), these results were already expected; however, for very short forecasts (for example, 1 and 2 min), our CNN shows improvements in forecasting cloud movement.

4.2. Analysis of the Simulation for All Simulated Datasets

Table 2 presents the statistical indicators of the cloud ROI changes in the 5000 tested images. Tables 1 and 2 show the quality of the results decreasing in forecasts for longer time scales, with *SD* values up to 44.4 ± 12.3% and *VO* of 37.7 ± 15.3% obtained for 10-min ahead forecasts.

4.3. Application of the Presented CNN Algorithm

To validate our algorithm, we applied an ANN as described in Section 3.4. For each predicted image from our CNN, the GHI value was predicted at the same time. Figure 4 shows a comparison between the target images and simulated images one-minute ahead generated as output by the CNN and their correspondent measured and simulated GHI.

Figure 5 shows the results for two examples of 10-min ahead simulations utilizing our method as an irradiance simulations tool. Table 3 shows a comparison between 100 observed images with their corresponding simulated values. Figure 6 shows the distribution of the relative deviations as a boxplot for different time horizons.
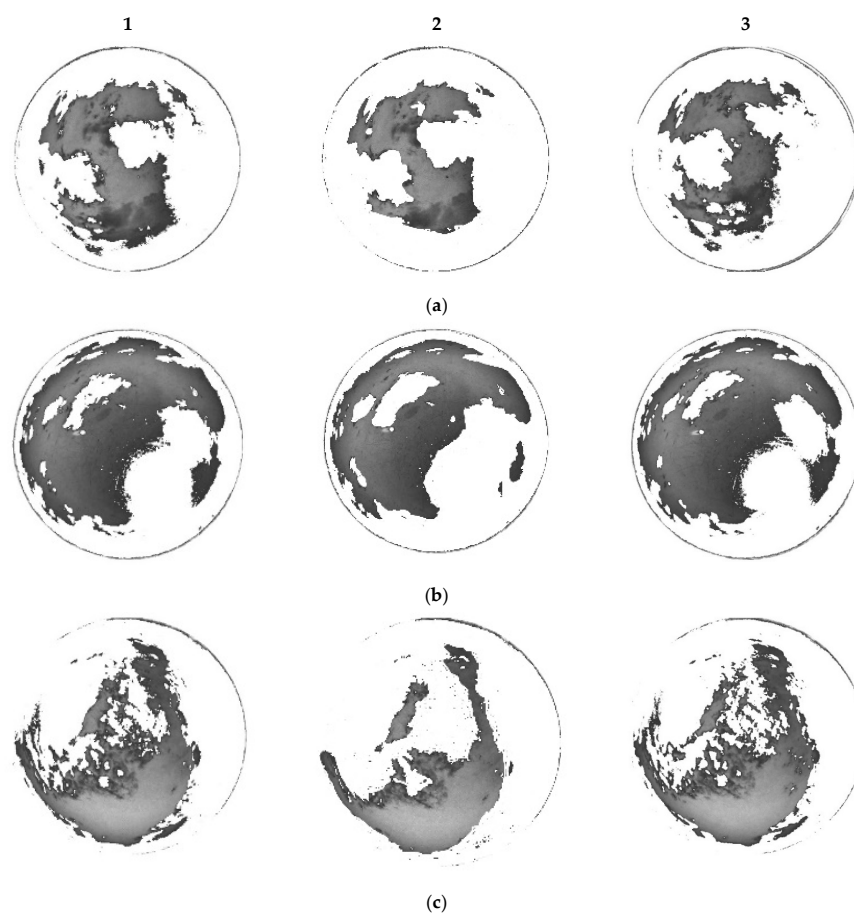
Figure 3. Cloud region of interest (ROI) changes forecasting results. Column 1 represents the target images in gray. Column 2 shows segmentation ROIs for the new model. The segmentation ROIs of the persistence model are presented in Column 3. (**a**) Images for 15 April 2014 at 15:54. (**b**) Images for 11 July 2014 at 13:09. (**c**) Images for 1 June 2014 at 17:42.

Table 1. Statistical indicators of the artificial neural network (ANN) model for four different time periods: the mean Sørensen–Dice similarity (*SD*) coefficient and the overlap (*VO*) for for 1-, 2-, 5-, and 10-min forecasts. CNN: convolutional neural network.

Day	Model	Statistical Parameters							
		SD (%)				*VO*(%)			
		1-min	2-min	5-min	10-min	1-min	2-min	5-min	10-min
24 March 2014 at 09:48	CNN	93	83	71	51	91	80	69	47
	Persistence	89	79	68	49	86	79	60	42
1 June 2014 at 17:37	CNN	92	82	69	57	90	81	62	49
	Persistence	88	78	64	52	84	75	57	43
24 May 2014 at 14:02	CNN	94	87	73	62	92	84	69	51
	Persistence	87	82	62	48	87	79	59	48
9 May 2015 at 15:26	CNN	87	79	62	51	85	78	57	46
	Persistence	83	71	58	49	80	70	55	40

Table 2. Comparison between the statistical indicators of the proposed CNN model and the persistence model: the mean Sørensen–Dice similarity coefficient (*SD*) and overlap (*VO*) of the 5000 simulated cases for 1-, 2-, 5-, and 10-min forecasts.

Model	Mean Statistical Parameters							
	SD (%)				*VO* (%)			
	1-min	2-min	5-min	10-min	1-min	2-min	5-min	10-min
CNN	94	83	60	49	92	80	58	43
Persistence	89	78	55	44	86	69	45	37

Original images with their measured GHI   **Simulated images with their measured GHI**

449 W/m²
(**a**)

457 W/m²
(**b**)

445 W/m²
(**c**)

438 W/m²
(**d**)

302 W/m²
(**e**)
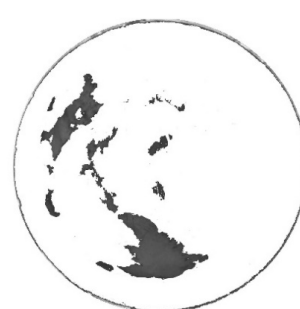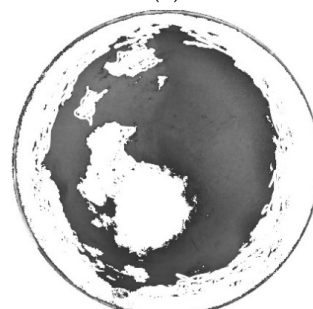
292 W/m²
(**f**)

Figure 4. Comparison between the observed images and simulated images one-minute ahead generated as output by the CNN and their correspondent measured and simulated global horizontal irradiance (GHI) values; (**a**) corresponds to 24 August 2014 at 09:45 with (**b**) as its simulations; (**c**) corresponds to 8 June 2015 at 15:10 with (**d**) as its simulations; (**e**) corresponds to 9 May 2017 at 10:42 with (**f**) as its simulations.
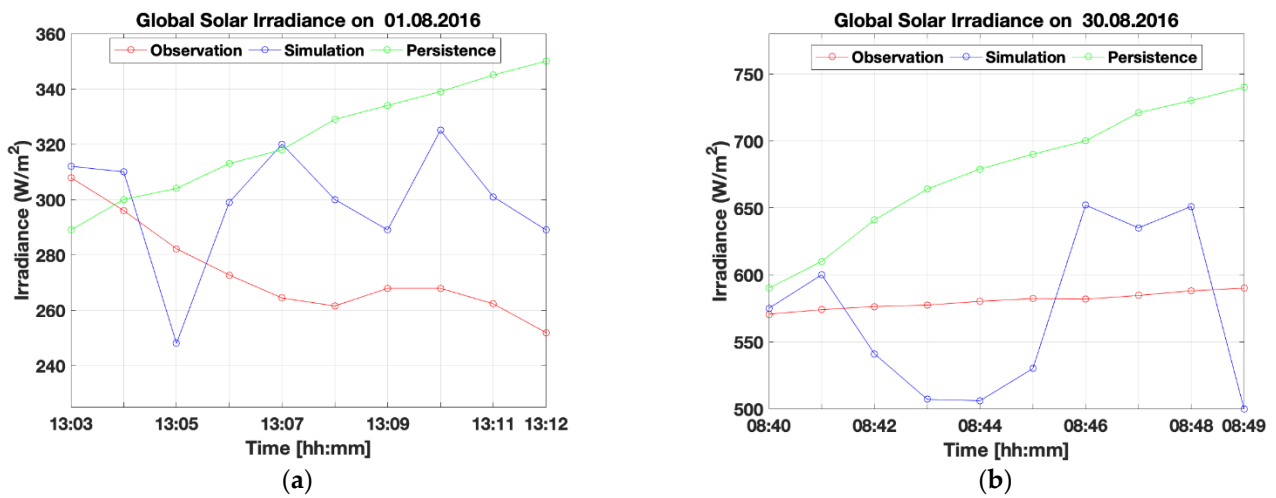
Figure 5. Comparison results of the simulation performed by the new and persistence model and the measured dataset at one-minute intervals; (**a**,**b**) show a good performance; $R^2 = 0.82$ and $R^2 = 0.74$, respectively, for the first two minutes. For the persistence model, $R^2 = 0.75$ and $R^2 = 0.67$, respectively, for the first two minutes.

Table 3. Presentation of the statistical indicator for the comparison between our model and the persistence model. *RMSE* and the R^2 of all 100 compared cases.

Model	Statistical Parameters							
	RMSE (W/m^2)(%)				R^2			
	1-min	2-min	5-min	10-min	1-min	2-min	5-min	10-min
CNN	32	54	101	148	0.81	0.65	0.53	0.42
Persistence	45	72	125	187	0.76	0.61	0.48	0.39
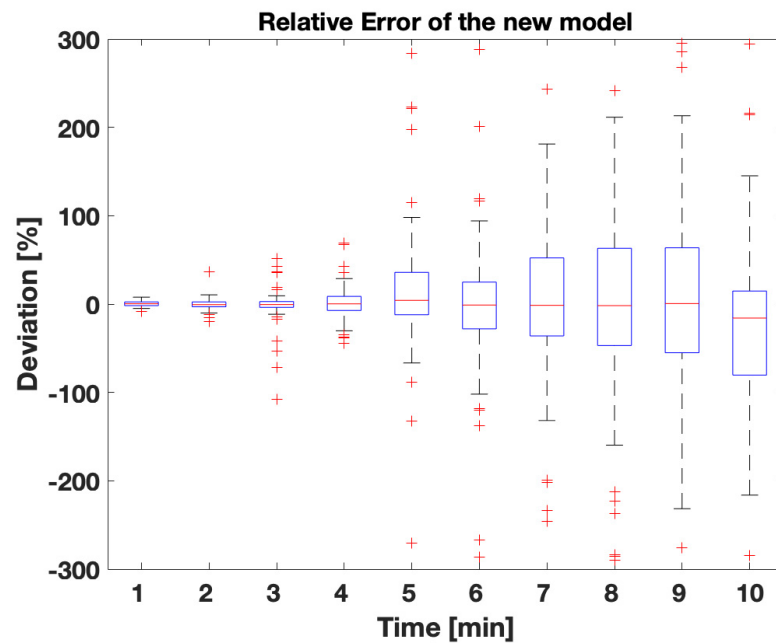
Figure 6. The mean relative deviation boxplot of all 782 simulation cases derived for different time horizons. The symmetry in 50% of the data decreases as soon as the program advances in time. Here, there are narrower interquartile ranges for higher sample sizes; symmetry in 50% of the data decreases as soon as the program receives more information, but the numbers of outliers (+) are lower.

5. Conclusions

In this study, a novel method to forecast cloud motion up to 10 min ahead was presented. A convolutional neural network (CNN) was trained using hemispherical sky images as inputs, and a statistical approach for forecasting future cloud motion was performed.

According to the simulation results, the method presented here is capable of predicting cloud changes for the first minute with very high confidence using CNN, with a coefficient of determination (R^2) of 0.97 and a Sørensen–Dice similarity coefficient (SD) of $94 \pm 2.6\%$. For the same simulated datasets, the persistence model reached an R^2 of 0.92 and a SD of $89 \pm 3.8\%$. The method was also tested for different forecast time scales, however, unsatisfactory results (an R^2 of 0.40 and a SD of $49 \pm 11.8\%$) were obtained for 10-min simulations by our model, although they were better than the results of the persistence model. In addition, the global horizontal irradiance (GHI) output results predicted by the CNN showed a forecast accuracy for the decreased amount of energy one-minute ahead, achieving a $RMSE$ of 32 (W/m^2) and a R^2 of 0.81. The persistence model achieved a $RMSE$ of 45 (W/m^2) and a R^2 of 0.76. However, for the GHI prediction for the next 10-min ahead, the $RMSE$ was 148 (W/m^2) and the R^2 was 0.42 for our model and the $RMSE$ was 187 (W/m^2) and the R^2 was 0.39 for the persistence model.

The research presented here can be used as a first step for PV companies to understand cloud movement and to implement an end-to-end forecasting system (as a pipeline) within a fully automated server with the goal of forecasting global horizontal irradiance minutes ahead. This fully automated pipeline implementation will help to allow PV companies to make accurate horizon time predictions and better marketing decisions for primary and secondary control reserves (i.e., up to 5 min in advance).

Future research is needed to better understand cloud movement through wind speed and wind direction, and also to understand how to improve forecast results for periods longer than 1 min or when the sky is totally covered. Different methodologies and maybe different analyses of data should be considered.

Despite the good results, the existence of other models offers new ways to process big data. For example, long short-term memory networks (LSTMs) appear to be an alternative. Since the architecture of these networks is more complex, LSTMs are suitable for processing long data sequences while avoiding vanishing or exploding gradients, currently problems that CNNs still have. As an outlook for further projects, the utilization of LSTM and hybrid models should be taken into consideration.

Author Contributions: Conceptualization, C.C. and E.W.L.; Data curation, C.C.; Formal analysis, C.C., E.W.L. and G.S.; Investigation, C.C.; Methodology, C.C.; Project administration, G.S.; Resources, G.S.; Software C.C.; Supervision, G.S.; Validation, C.C. and E.W.L.; Visualization, C.C. and G.S.; Writing–original draft, C.C. and E.W.L. All authors have read and agreed to the published version of the manuscript.

Institutional Review Board Statement: Not applicable.

Informed Consent Statement: Not applicable.

Data Availability Statement: Not applicable.

Conflicts of Interest: The authors declare no conflict of interest.

References

1. Chauvin, R.; Nou, J.; Thil, S.; Grieu, S. Cloud motion estimation using a sky imager. *AIP Conf. Proc.* **2016**, *1734*, 150003.
2. Dev, S.; Savoy, F.M.; Lee, Y.H.; Winkler, S. Short-term prediction of localized cloud motion using ground-based sky imagers. In Proceedings of the Region 10 Conference (TENCON), Singapore, 22–25 November 2016; pp. 2563–2566.
3. Kleissl, J. *Solar Energy Forecasting and Resource Assessment*, 1st ed.; Elsevier: Amsterdam, The Netherlands, 2013.

4. Marquez, R.; Coimbra, C.F.M. Intra-hour DNI forecasting based on cloud tracking image analysis. *Sol. Energy* **2013**, *91*, 327–336. [CrossRef]

5. Dissawa, D.M.L.H.; Ekanayake, M.P.B.; Godaliyadda, G.M.R.I.; Ekanayake, J.B.; Agalgaonkar, A.P. Cloud motion tracking for short-term on-site cloud coverage prediction. In Proceedings of the 17th International Conference on Advances in ICT for Emerging Regions (ICTer), Colombo, Sri Lanka, 6–9 September 2017; Proc. 2018-Janua. pp. 332–337. [CrossRef]

6. Volker Quaschning. Statistiken. 2017. Available online: https://www.volker-quaschning.de/datserv/pv-welt/index.php (accessed on 24 October 2019).

7. Escrig, H.; Batlles, F.J.; Alonso, J.; Baena, F.M.; Bosch, J.L.; Salbidegoitia, I.B.; Burgaleta, J.I. Cloud detection, classification and motion estimation using geostationary satellite imagery for cloud cover forecast. *Energy* **2013**, *55*, 853–859. [CrossRef]

8. Huang, H.; Xu, J.; Peng, Z.; Yoo, S.; Yu, D.; Huang, D.; Qin, H. Cloud motion estimation for short term solar irradiation prediction. In Proceedings of the 2013 IEEE International Conference on Smart Grid Communications (SmartGridComm), Vancouver, BC, Canada, 21–24 October 2013; pp. 696–701. [CrossRef]

9. Dev, S.; Lee, Y.H.; Winkler, S. Color-Based Segmentation of Sky/Cloud Images From Ground-Based Cameras. *IEEE J. Sel. Top. Appl. Earth Obs. Remote Sens.* **2016**, 1–12. [CrossRef]

10. Kreuter, A.; Zangerl, M.; Schwarzmann, M.; Blumthaler, M. All-sky imaging: A simple, versatile system for atmospheric research. *Appl. Opt.* **2009**, *48*, 1091–1097. [CrossRef]

11. Heinle, A.; Macke, A.; Srivastav, A. Automatic cloud classification of whole sky images. *Atmos. Meas. Tech.* **2010**, *3*, 557–567. [CrossRef]

12. Yang, J.; Lu, W.; Ma, Y.; Yao, W. An automated cirrus cloud detection method for a ground-based cloud image. *J. Atmos. Ocean. Technol.* **2012**, *29*, 527–537. [CrossRef]

13. Long, C.N.; Sabburg, J.M.; Calbó, J.; Pagès, D. Retrieving cloud characteristics from ground-based daytime color all-sky images. *J. Atmos. Ocean. Technol.* **2006**, *23*, 633–652. [CrossRef]

14. Liu, S.; Zhang, L.; Zhang, Z.; Wang, C.; Xiao, B. Automatic cloud detection for all-sky images using superpixel segmentation. *IEEE Geosci. Remote Sens. Lett.* **2015**, *12*, 354–358.

15. Kumler, A.; Xie, Y.; Zhang, Y. *A New Approach for Short-Term Solar Radiation Forecasting Using the Estimation of Cloud Fraction and Cloud Albedo*; Report Number NREL/TP-5D00-72290; National Renewable Energy Laboratory: Golden, CO, USA, 2018.

16. Yang, J.; Lv, W.T.; Ma, Y.; Yao, W.; Li, Q.Y. An automatic groundbased cloud detection method based on adaptive threshold. *J. Appl. Meteorol. Sci.* **2009**, *20*, 713–721.

17. Cazorla, A.; Olmo, F.J.; Alados-Arboledas, L. Development of a sky imager for cloud cover assessment. *J. Opt. Soc. Am. A.* **2008**, *25*, 29–39. [CrossRef] [PubMed]

18. Ren, X.F.; Malik, J. Learning a classification model for segmentation. In Proceedings of the 9th IEEE International Conference on Computer Vision, Nice, France, 13–16 October 2003; pp. 10–17.

19. Peng, B.; Zhang, L.; Zhang, D. Automatic image segmentation by dynamic region merging. *IEEE Trans. Image Process.* **2011**, *20*, 3592–3605. [CrossRef] [PubMed]

20. Le Goff, M.; Tourneret, J.; Wendt, H.; Ortner, M.; Spigai, M. Deep learning for cloud detection. In Proceedings of the ICPRS 8th International Conference of Pattern Recognition Systems, Madrid, Spain, 11–13 July 2017; pp. 1–6.

21. Malek, E. Evaluation of effective atmospheric emissivity and parameterization of cloud at local scale. *Atmos. Res.* **1997**, *45*, 41–54. [CrossRef]

22. Jiménez-Pérez, P.; López, L. Modeling and forecasting hourly global solar radiation using clustering and classification techniques. *Sol. Energy* **2016**, *135*, 682–691. [CrossRef]

23. Li, Z.; Shen, H.; Cheng, Q.; Liu, Y.; You, S.; He, Z. Deep learning based cloud detection for medium and high resolution remote sensing images of different sensors. *ISPRS J. Photogramm. Remote Sens.* **2019**, *150*, 197–212. [CrossRef]

24. Onishi, R.; Sugiyama, D. Deep convolutional neural network for cloud coverage estimation from snapshot camera images. *SOLA* **2017**, *13*, 235–239. [CrossRef]

25. Crisosto, C. Autoregressive Neural Network for Cloud Concentration Forecast from Hemispheric Sky Images. *Int. J. Photoenergy* **2019**, *2019*, 4375874, 8 pages. [CrossRef]

26. Crisosto, C.; Hofmann, M.; Mubarak, R.; Seckmeyer, G. One-Hour Prediction of the Global Solar Irradiance from All-Sky Images Using Artificial Neural Networks. *Energies* **2018**, *11*, 2906. [CrossRef]

27. Moncada, A.; Richardson, W.; Vega-Avila, R. Deep learning to forecast solar irradiance using a six-month UTSA SkyImager dataset. *Energies* **2018**, *11*, 1988. [CrossRef]

28. Sun, Y.; Venugopal, V.; Brandt, A.R. Convolutional Neural Network for Short-term Solar Panel Output Prediction. In Proceedings of the 2018 IEEE 7th World Conference on Photovoltaic Energy Conversion (WCPEC) (A Joint Conference of 45th IEEE PVSC, 28th PVSEC & 34th EU PVSEC), Waikoloa Village, HI, USA, 10–15 June 2018; pp. 2357–2361.

29. Siddiqui, T.A.; Bharadwaj, S.; Kalyanaraman, S. A deep learning approach to solar-irradiance forecasting in sky-videos. In Proceedings of the IEEE Winter Conference on Applications of Computer Vision (WACV), Waikoloa Village, HI, USA, 7–11 January 2019; pp. 2166–2174.

30. Tohsing, K.; Schrempf, M.; Riechelmann, S.; Schilke, H.; Seckmeyer, G. Measuring high-resolution sky luminance distributions with a CCD camera. *Appl. Opt.* **2013**, *52*, 1564–1573. [CrossRef]

31.　Anon. CMP11 Pyranometer. Available online: http://www.kippzonen.com/Product/13/CMP11-Pyranometer#.WXi1sK3qh-U (accessed on 23 May 2018).

32.　Yamashita, M.; Yoshimura, M.; Nakashizuka, T. Cloud Cover Estimation using Multitemporal Hemisphere Imageries. *Inter. Arch. Photogramm. Remote Sens. Spat. Inf. Sci.* **2004**, *35*, 826–829.

33.　Schrempf, M. Entwicklung eines Algorithmus zur Wolkenerkennung in Digitalbildern des Himmels. Master's Thesis, Institut für Meteorologie und Klimatologie, Hanover, Germany, 2012.

34.　Simonyan, K.; Zisserman, A. Very Deep Convolutional Neural Networks for Large-Scale Image Recognition. In Proceedings of the International Conference on Learning Representations, San Diego, CA, USA, 7–9 May 2015.

35.　He, K.; Zhang, X.; Ren, S.; Sun, J. Delving deep into rectifiers: Surpassing human-level performance on ImageNet classification. *arXiv* **2015**, arXiv:1502.01852 Cs.

36.　Kingma, D.P.; Ba, J. Adam: A method for stochastic optimization. *arXiv* **2014**, arXiv:1412.6980 Cs.

37.　Zou, K.H.; Warfield, S.K.; Bharatha, A.; Tempany, C.M.; Kaus, M.R.; Haker, S.J.; Wells, W.M., III; Jolesz, F.A.; Kikinis, R. Statistical validation of image segmentation quality based on a spatial overlap index. *Acad. Radiol.* **2004**, *11*, 178–189. [CrossRef]

38.　Stegmann, M.B.; Delgado, D. A Brief Introduction to Statistical Shape Analysis. Informatics and Mathematical Modelling. March 2002. 15p. Available online: http://graphics.stanford.edu/courses/cs164-09-spring/Handouts/paper_shape_spaces_imm403.pdf (accessed on 1 January 2021).

39.　Notton, G.; Voyant, C. Forecasting of Intermittent Solar Energy Resource. In *Advances in Renewable Energies and Power Technologies*; Elsevier: Amsterdam, The Netherlands, 2018; Volume 1, pp. 77–114. [CrossRef]

40.　Wilks, D.S. *Statistical Methods in the Atmospheric Sciences*; Academic Press: Cambridge, MA, USA, 2011.

5 Conclusions

5.1 Summary of the results

The main goal of the present thesis was the prediction of the solar irradiance one-hour ahead under diverse weather conditions. To realize this goal, an autoregressive neural network with backpropagation (Ar-BP), a feed-forward neural network with Levenberg-Marquardt Backpropagation (LM-BP) and a convolutional neural network (CNN) were implemented. The pictures were recorded by a hemispheric sky imager (HSI) at the Institute of Meteorology and Climatology (IMuK) of the Leibniz University Hannover, Hannover, Germany.

The results of the Ar-BP neural network show that the model makes a significant progress to predict cloud concentration five minutes in advance using a machine learning method, outperforming the persistence solar model by approximately 30%. In order to support accurate solar irradiance forecasts and the horizon time prediction of this algorithm, the proposed cloud concentration forecast method can be used as a tool for solar energy forecasts and could play an important role in German markets and within the European Union as well. Furthermore, the Ar-BP was extended to a new solar irradiance prediction method developed to forecast one hour ahead. The GHI predicted by the proposed methodology improves the forecast for the total amount of energy one hour ahead by reducing both the $RMSE$ and MAE of the simulation by approximately 40% when compared to the persistence solar model. Furthermore, the results have shown that the new model is capable of reproducing the nonlinear nature of the solar irradiance more reliably than statistical linear models. It is also worth mentioning that for irradiation levels under $80 - 100W/m^2$, the new algorithm does not accurately predict one hour ahead. However, such low irradiances are usually not relevant for the production of solar energy. Nevertheless, for higher irradiance the new algorithm can predict one hour ahead under diverse weather conditions with an average deviation of 22% within the next hour.

As stated by Yang [66], the forecast methods presented in this work match the relationship accuracy of solar forecasts, which varies across locations and time periods. Thus, the both RMSE and MAE were chosen for the forecast as meteorological metrics. In addition, Yang defined "climatology" and "persistence" as two commonly used and benchmarks models differing only in the forecast goal. Therefore, as established by Yang and for determining the "skill" factor, the proposed work considered the persistence solar method as benchmark model to be compared with the created ANN model.

Furthermore, according to the simulation results of the CNN, it was possible to predicting cloud changes for the first minute with very high confidence with a coefficient of determination (R^2) of 0.97 and a Sørensen-Dice similarity coefficient (SCD) of $94 \pm 2.6\%$. For the same simulated datasets, the persistence solar model reached an R^2 of 0.92 and a SCD of $89 \pm 3.8\%$. The method proposed here was also tested for different forecast time scales, however, unsatisfactory results (R^2 of 0.40 and a SCD of $49 \pm 11.8\%$) were obtained for 10-min simulations. In addition, the developed CNN was also utilized as a validation method for the outputs results of the GHI prediction algorithm. Thus, the CNN showed a forecast accuracy for the decreased amount of energy one-minute ahead, achieving a mean $RMSE$ of $32(W/m^2)$ and a R^2 of 0.81. The persistence solar model achieved a mean $RMSE$ of $45(W/m^2)$ and a R^2 of 0.76. However, for the GHI prediction for the next 10-min ahead, the mean $RMSE$ was $148(W/m^2)$ and the R^2 was 0.42 for our model and the $RMSE$ was $187(W/m2)$ and the R^2 was 0.39 for the persistence solar model.

In conclusion, the research presented here could be used as a first step for PV companies to understand cloud movement, to predict GHI and to implement an end-to-end solar forecasting system (as a pipeline) within a fully automated server with the goal of forecasting GHI minutes ahead. This fully automated pipeline implementation would help to allow PV companies to make accurate horizon time predictions and better marketing decisions for primary and secondary control reserves.

5.2 Limitations

Despite to the good results, the model presented here has only been tested for the location at Herrenhausen, Hannover, Germany in the period from 2012 until 2016. The neural network may be trained with datasets from other places. To achieve this, only the pictures of the desired place with the respective pyranometer measurements are sufficient. The existence of other models offers new ways to process big data, as well. For example, long short-term memory networks (LSTMs) appear to be an alternative. Since the architecture of these networks is more complex, LSTMs are suitable for processing long data sequences while avoiding vanishing or exploding gradients, currently problems that CNNs still have.

6 Outlook

In the future, in order to further improve the performance of the novel model presented here some topics need to be addressed.

- The model has only been tested at IMuK. The neural network could be trained with datasets from other locations. To achieve this, only the pictures of the desired place with the respective pyranometer measurements are sufficient.

- To make the ANN "more intelligent". The ANN proposed in this thesis has training data from 2012 to 2016. Extra data from both the all-sky images and the pyranometer from the same location will be necessary for a new training datasets, and thus, to increase the network's process of recognition of new patterns.

- Electricity grid. This work could be especially relevant for implementing strategies in decisions for the balance of supply and demand of electricity. An array of all-sky camera devices would help to extend the temporal and spatial information of the sky for better predictions and also better estimations of power output by avoiding variation in the electrical grid.

- Improvement of simulated cloud images. The improvement of the algorithm to predict cloud images could be upgraded by adding new photos for the training of the neural network. This algorithm can be important for solar energy supplier companies to get a better prediction of cloud images not just a minute but rather a few minutes ahead. In addition, this algorithm should also be tested with all-sky images from other places.

Besides these proposed improvements, the new ANN model may serve as a basis for further projects at IMuK. In addition, a several tests should be planned in Hannover, Germany and other places.

Thus, the proposed thesis shows that it is already possible to carry out simulations with the new GHI prediction method with acceptable deviations overcoming existing linear models.

Bibliography

[1] Die Bundesregierung (2017): *Energiekonzept 2050*. [Homepage] [17.07.2017]. URL: https://www.bundesregierung.de/Content/DE/HTML/Breg/Anlagen/infografik-energie-textversion.html.

[2] Bundesnetzagentur (2017): PV-Datenmeldungen und EEG-Verg ütungssätze. [Homepage][17.07.2017]. URL: https://www.bundesnetzagentur.de

[3] Bundesnetzagentur (2013). Available online: https://www.bundesnetzagentur.de (accessed on 17 February 2018).

[4] Volker Quaschning (2017): Statistiken. 2007. Available online: https://www.volker-quaschning.de/datserv/pv-welt/index.php (accessed on 9 February 2018).

[5] Hofmann, M., Riechelmann, S., Crisosto, C., Mubarak, R., & Seckmeyer, G. (2014). *Improved synthesis of global irradiance with one-minute resolution for PV system simulations.* International Journal of Photoenergy, 2014.

[6] IEA,InternationalEnergyAgency,WorldEnergyOutlook2016, Executive Summary, International Energy Agency, World Energy Outlook, 2016, http://www.iea.org (accessed on 17 February 2018).

[7] Umweltbundesamt (2017): *Erneuerbare Energien in Zahlen.* [Homepage] [17.07.2017]. URL: http://www.umweltbundesamt.de/themen/klima-energie/erneuerbare-energien/erneuerbare-energien-in-zahlen-strom.

[8] Ant., Gil, J.E., Cazorla, A., Fernez-Gez, J., Foyo-Moreno, I., Olmo, F.J., Alados-Arboledas, L., 2011. *Short-term variability of experimental ultraviolet and total solar irradiance in Southeastern Spain.* Atmos. Environ. 45, 4815?4821. https://doi.org/10.1016/j.atmosenv.2011.06.020.

[9] Tohsing, K., Schrempf, M., Riechelmann, S., Schilke, H., Seckmeyer, G. (2013). *Measuring high-resolution sky luminance distributions with a CCD camera.* Appl. Opt., 52(8), 1564?1573.

[10] Yamashita, M.; Yoshimura, M.; Nakashizuka, T. *Cloud Cover Estimation using Multitemporal Hemisphere Imageries.* Inter. Arch. Photogramm. Remote Sens. Spat. Inf. Sci. 2004, 35, 826?829.

[11] Vaisala Energy (2018): Glossary of Technical Renewable Energy Terminology [Online]

https://www.3tier.com/en/support/glossary/ghi

[12] Anon. Available online: http://www.kippzonen.com/Product/13/CMP11-Pyranometer.WXi1sK3qh-U (accessed on 23 May 2018).

[13] Estimation, F. Full Vectorization of Solar Azimuth and Elevation Estimation-File Exchange-MATLAB Central. Available online: https://de.mathworks.com/matlabcentral/fileexchange/48594-full-vectorization-of-solarazimuth-and-elevation-estimation (accessed on 21 July 2015).

[14] Li, Y.; Su, Y.; Shu, L. An ARMAX model for forecasting the power output of a grid-connected photovoltaic system. Renew. Energy 2014, 66, 78?89.

[15] Liou, K.N., 2002. *An Introduction to Atmospheric Radiation (Google eBook)*, International Geophysics.

[16] Malek, E., 1997. *Evaluation of effective atmospheric emissivity and parameterization of cloud at local scale.* Atmos. Res. 45, 41?54. https://doi.org/10.1016/S0169-8095(97)00020-3.

[17] Calb, 2005. *Empirical studies of cloud effects on UV radiation: A review.* Rev. Geophys. 43, RG2002. https://doi.org/10.1029/2004RG000155.

[18] Tzoumanikas, P., Nikitidou, E., Bais, A.F., Kazantzidis, A., 2016. *The effect of clouds on surface solar irradiance, based on data from an all-sky imaging system.* Renew. Energy 95, 314?322. https://doi.org/10.1016/j.renene.2016.04.026.

[19] Werkmeister, A., Lockhoff, M., Schrempf, M., Tohsing, K., Liley, B., Seckmeyer, G., 2015. *Comparing satellite- to ground-based automated and manual cloud coverage observations - A case study.* Atmos. Meas. Tech. 8, 2001?2015. https://doi.org/10.5194/amt-8-2001-2015.

[20] C. N. Long, J. M. Sabburg, J. Calbd D. Pag Retrieving cloud characteristics from ground-based daytime color all-sky images J. Atmos. Ocean. Technol., vol. 23, no. 5, pp. 633?652, May 2006.

[21] A. Kreuter, M. Zangerl, M. Schwarzmann, and M. Blumthaler, *All-sky imaging: A simple, versatile system for atmospheric research*, Appl. Opt., vol. 48, no. 6, pp. 1091?1097, Feb. 2009.

[22] A. Heinle, A. Macke, and A. Srivastav, *Automatic cloud classification of whole sky images*, Atmos. Meas. Technol., vol. 3, no. 1, pp. 557?567, May 2010.

[23] Liu, S., Zhang, L., Zhang, Z., Wang, C., Xiao, B. (2015). *Automatic cloud detection for all-sky images using superpixel segmentation.* IEEE Geoscience and Remote Sensing Letters, 12(2), 354?358.

[24] Kumler, Andrew, Yu Xie, and Yingchen Zhang. 2018. *A New Approach for Short-Term Solar Radiation Forecasting Using the Estimation of Cloud Fraction and Cloud Albedo.* Golden, CO: National Renewable Energy Laboratory. NREL/TP-5D00-72290.

[25] J. Yang, W. T. Lv, Y. Ma, W. Yao, and Q. Y. Li, *An automatic groundbased cloud detection method based on adaptive threshold*, J. Appl. Meteorol. Sci., vol. 20, no. 6, pp. 713?721, 2009.

[26] Cazorla, A., Olmo, F. J., and Alados-Arboledas, L., 2008. *Development of a sky imager for cloud cover assessment.* J. Opt. Soc. Am. A. 25, 29-39.

[27] X. F. Ren and J. Malik, *Learning a classification model for segmentation*, in Proc. 9th IEEE Int. Conf. Comput. Vis., 2003, pp. 10?17.

[28] B. Peng, L. Zhang, and D. Zhang, *Automatic image segmentation by dynamic region merging*, IEEE Trans. Image Process., vol. 20, no. 12, pp. 3592?3605, Dec. 2011.

[29] S. Liu, L. Zhang, Z. Zhang, C. Wang, and B. Xiao, *Automatic cloud detection for all-sky images using superpixel segmenta- tion*, IEEE Geoscience and Remote Sensing Letters, vol. 12, no. 2, pp. 354?358, 2015.

[30] E. Scolari, F. Sossan, and M. Paolone, *Irradiance prediction intervals for PV stochastic generation in microgrid applications*, Solar Energy, vol. 139, pp. 116?129, 2016.

[31] R. Marquez and C. F. M. Coimbra, *Intra-hour DNI forecasting based on cloud tracking image analysis*, Solar Energy, vol. 91, pp. 327?336, 2013.

[32] Matthieu Le Goff, Jean-Yves Tourneret, Herwig Wendt, Mathias Ortner, Marc Spigai. *Deep learning for cloud detection.* ICPRS (8th International Conference of Pattern Recognition Systems), Jul 2017, Madrid, Spain. 8th International Conference of Pattern Recognition Systems (ICPRS 2017), pp. 1-6, 2017.

[33] Onishi, R., and D. Sugiyama, 2017: *Deep convolutional neural network for cloud coverage estimation from snapshot camera images.* SOLA, 13, 235?239, doi:10.2151/sola.2017-043.)

[34] J. O. Kamadinata, T. Lit Ken, and T. Suwa, *Global solar radiation prediction methodology using artificial neural networks for photovoltaic power generation systems*, in Proceedings of the 6th International Conference on Smart Cities and Green ICT Systems - Volume 1: SMARTGREENS, Porto, Portugal, 2017.

[35] Z. Zhen, Z. Wang, F. Wang, Z. Mi, and K. Li, *Research on a cloud image forecasting approach for solar power forecasting*, Energy Procedia, vol. 142, pp. 362?368, 2017.

[36] Cristian Crisosto, *Autoregressive Neural Network for Cloud Concentration Forecast from Hemispheric Sky Images*, International Journal of Photoenergy, vol. 2019, Article ID 4375874, 8 pages, 2019. https://doi.org/10.1155/2019/4375874.

[37] Crisosto, C.; Hofmann, M.; Mubarak, R.; Seckmeyer, G. *One-Hour Prediction of the Global Solar Irradiance from All-Sky Images Using Artificial Neural Networks.* Energies 2018, 11, 2906.

[38] Almeida, M.P.; Perpin O.; Navarrete, L. *PV power forecast using a nonparametric PV model.* Sol. Energy 2015, 115, 354?368.

[39] Amrouche, B.; Sicot, L.; Guessoum, A.; Belhamel, M. *Experimental analysis of the maximum power point?s properties for four photovoltaic modules from different technologies*: Monocrystalline and polycrystalline silicon, CIS and CdTe. Sol. Energy Mater. Sol. Cells 2013.

[40] Thapar, V.; Agnihotri, G.; Sethi, V.K. *Estimation of Hourly Temperature at a Site and its Impact on Energy Yield of a PV Module.* Int. J. Green Energy 2012, 9, 553?572.

[41] Thapar, V. *A revisit to solar radiation estimations using sunshine duration: Analysis of impact of these estimations on energy yield of a PV generating system.* Energy Sources Part A Recovery Util. Environ. Eff. 2019, 1?25.

[42] Tsay, R.S. *Analysis of Financial Time Series Second Edition*; John Wiley Sons: New York, NY, USA, 2005.

[43] Creal, D.; Koopman, S.; Lucas, A. *Generalized autoregressive score models with applications.* J. Appl. Econom. 2013, 28, 777?795.

[44] Qing, X.; Niu, Y. *Hourly day-ahead solar irradiance prediction using weather forecasts by LSTM.* Energy 2018, 148, 461?468.

[45] Li, S.; Jin, X.; Xuan, Y.; Zhou, X.; Chen, W.; Wang, Y.X.; Yan, X. *Enhancing the Locality and Breaking the Memory Bottleneck of Transformer on Time Series Forecasting.* Adv. Neural Inf. Process. Syst. 2020, 5243?5253.

[46] Wang, Y.; Shen, Y.; Mao, S.; Chen, X.; Zou, H. *LASSO LSTM Integrated Temporal Model for Short-term Solar Intensity Forecasting.* IEEE Internet Things J. 2018.

[47] Shih, S.; Sun, F.; Lee, H.Y. *Temporal pattern attention for multivariate time series forecasting.* Mach. Learn. 2019, 108, 1421?1441.

[48] Wilks, D.S. *Statistical Methods in the Atmospheric Sciences*; Academic Press: Cambridge, MA, USA, 2011.

[49] Richard, P.; Sergey, K.; James, S.; Karl, H.J.; David, R.; Thomas, E.H. *Validation of short and medium term operational solar radiation forecasts in the US.* Sol. Energy 2010, 84, 2161?2172.

[50] Mellit, A.; Kalogirou, S.A. *Artificial intelligence techniques for photovoltaic applications: A review.* Prog. Energy Combust. Sci. 2008, 34, 547?632.

[51] Hochreiter, S.; Schmidhuber, J. *Long Short-Term Memory. Neural Comput.* 1997, 9, 1735?1780.

[52] Srivastava, S.; Lessmann, S. *A comparative study of LSTM neural networks in forecasting day-ahead global horizontal irradiance with satellite data.* Sol. Energy 2018, 162, 232?247.

[53] Brockwell, P.; Davis, R. *Introduction to Time Series and Forecasting*Second Edition; Springer: Berlin/Heidelberg, Germany, 2002.

[54] Seckmeyer, G., et al., 2010: Instruments to measure solar ultraviolet radiation, part 4: Array spectroradiometers. Tech. rep., World Meteorological Organization.

[55] Azevedo, F. A. et al. (2009) Equal numbers of neuronal and nonneuronal cells make the human brain an isometrically scaled-up primate brain.

[56] He, K.; Zhang, X.; Ren, S.; Sun, J. Delving deep into rectifiers: Surpassing human-level performance on ImageNet classification. arXiv 2015, arXiv:1502.01852 Cs.

[57] Simonyan, K. Zisserman, A. Very deep convolutional networks for large-scale image recognition. 3rd Int. Conf. Learn. Represent. ICLR 2015 - Conf. Track Proc. 1?14 (2015).

[58] Jiang, Y.; Cheng, W.; Gao, F.; Zhang, S.; Wang, S.; Liu, C.; Liu, J. A Cloud Classification Method Based on a Convolutional Neural Network for FY-4A Satellites. Remote Sens. 2022,14,2314. https://doi.org/ 10.3390/rs14102314

[59] Droenner, Johannes Korfhage, Nikolaus Egli, Sebastian Muehling, Markus Thies, Boris Bendix, Jrg Freisleben, Bernd Seeger, Bernhard. (2018). Fast Cloud Segmentation Using Convolutional Neural Networks. Remote Sensing. 10. 1782. 10.3390/rs10111782.

[60] Gu, Jiuxiang Wang, Zhenhua Kuen, Jason Ma, Lianyang Shahroudy, Amir Shuai, Bing Liu, Ting Wang, Xingxing Wang, Gang. (2015). Recent Advances in Convolutional Neural Networks. Pattern Recognition. 77. 10.1016/j.patcog.2017.10.013.

[61] Schrempf, M. *Entwicklung eines Algorithmus zur Wolkenerkennung in Digitalbildern des Himmels.* Master?s Thesis, Institut fr Meteorologie und Klimatologie, Hanover, Germany, 2012.

[62] D. S. Wilks, *Statistical Methods in the Atmospheric Sciences*, Academic Press, Cambridge, MA, USA, 2011.

[63] M. P. Almeida, O. Perpi and L. Narvarte, *PV power fore- cast using a nonparametric PV model*, Solar Energy, vol. 115, pp. 354?368, 2015.

[64] Yamashita, R., Nishio, M., Do, R.K.G. et al. Insights Imaging (2018) 9: 611. https://doi.org/10.1007/s13244-018-0639-9.

[65] Stegmann, M. B., Delgado, D. (2002). A brief introduction to Statistical Shape Analysis. Informatics and Mathematical Modelling, (March), 15 pp.

[66] Yang, H.Y.; Ye, H.; Wang, G.Z. Applications of chaos theory to load forecasting in power system. Relay 2005, 33, 26?30.

[67] Serrano, A., Soria, E., (2009-2010) Curso 2009-2010 pag. 8-13-14-72. Programa 3er ciclo (Doctorado) Escola Tecnica Superior dEnginyeria. Valencia.

[68] McCarthy. J., Hayes, Patrick (1969) Some Philosophical Problems from the Standpoint of Artificial Intelligence. Stanford 1969.

[69] Haykin, Simon S. (1999): Neural networks. A comprehensive foundation. 2nd pag 30-200.

Upper Saddle River, N.J: Prentice Hall.

[70] Coello. A., Castillejo. M., (2002): Dispepsia y redes neuronales. Publicado en Aten Primaria. 2002;30:665. - vol.30 núm 10. Available at http://www.elsevier.es/es/revistas/atentcion-primaria-27/dispepsia-redes-neuronales-13041215-cartas-al-director-2002.

[71] Rumelhart. D., Hinton. G., Williams. R., in Pararell Distribuided Processing: Explorations in the Microestructure of Cognition. Vol 1: 318-362 (MIT. Cambridge, 1986).

[72] Kramer, M. A., Leonard, J. (1990) Improvement of the backpropagation algorithm for training neural networks. Computers and Chemical Engineering. http://doi.otg/10.1016/0098-1354(90)87070-6.

[73] Rojas, Raúl (1996): Neural networks - A systematic introduction. Springer. http://doi.org/10.1016/0893-6080(94)90051-5.

[74] Haykin, Simon. (1999): Neural networks: a comprehensive foundation by Simon Haykin. The Knowledge Engineering Review. http://doi.org/10.1017/S02698888998214044.

[75] Gordon Reikard (2009): Predicting solar radiation at high resolutions: A comparison of time series forecasts. Solar Energy, 83: 342-349.

[76] Maimouna Diagne (2013): Review of solar irradiance forecasting methods and a proposition for small-scale insular grids. Renewable and Sustainable Energy Reviews, 27: 65-76.

[77] Jan Remund und Richard Perez (2008): Comparison of solar radiation forecasts for the USA. Valencia. 23rd European Photovoltaic and Solar Energy Conference and Exhibition.

[78] Elke Lorenz (2004): Methoden zur Beschreibung der Wolkenentwicklung in Satellitenbildern und ihre Anwendung zur Solarstrahlungsvorhersage. Oldenburg: Carl von Ossietzky Universit ät.

[79] Richard Perez et al (2010): Validation of short and medium term operational solar radiation forecasts in the US. Solar Energy, 84: 2161-2172.

[80] Werkmeister A., Lockhoff M., Schrempf M., Tohsing K., Liley B., Seckmeyer G. (2013) Comparing satellite to ground based automated and manual cloud coverage observations a case study, Atmospheric Measurement Techniques

[81] Chi Wai Chow et al (2011): Intra-hour forecasting with a Total Sky Imager at the UC San Diego solar energy testbed. San Diego: University of California, Department of Mechanical and Aerospace Engineering.

[82] Hadja Maïmouna Diagne et al (2013): Solar irradiation forecasting: state of the art and proposition for future development for small-scale insular grids. Renewable and Sustainable Energy Reviews, 28: 65-76.

[83] International Energy Agency: https://www.iea.org/etp/

[84] Peter Cramton; *Electricity market design*, Oxford Review of Economic Policy, Volume 33, Issue 4, 2 November 2017, Pages 589-612, https://doi.org/10.1093/oxrep/grx041

[85] http://www.solarpowereurope.org/wp-content/uploads/2018/09/Global-Market-Outlook-2018-2022.pdf

[86] http://www.ren21.net/wp-content/uploads 2018/06/17-8652-GSR2018-FullReport-web-final-.pdf

[87] Wang F, Mi Z, Su S, Zhao H. Short-term solar irradiance forecasting model based on artificial neural network using statistical feature parameters. Energies 2012;5:1355-70. doi:10.3390/en5051355.

[88] Wang F, Xu H, Xu T, Li K, Shafie-khah M, Catalao JPS. The values of market-based demand response on improving power system reliability under extreme circumstances. Appl energy 2017;193:220-31. doi:10.1016/j.apenergy.2017.01.103.

[89] Michael Schrempf: "Entwicklung eines Algorithmus zur Wolkenerkennung in Digitalbildern des Himmels". Diploma Thesis at IMuK 2012.

[90] Li J, Lu B-L. An adaptive image Euclidean distance. Pattern Recognition 2009; 42:349-57. doi:10.1016/j.patcog.2008.07.017.

Acknowledgements

First of all, I would like to thank the main support in my life, God.

My most sincere thanks to Professor Dr. Gunther Seckmeyer for his unconditional support both professionally and privately. I remember a couple of very nutritive conversations in his office which were the fundamental pillars of my professional life. Also, I want to thank him for the time I was in IMuK and for his infinite patience. I owe him one!

Prof. Dr. Michael Altenbuchinger, Prof. Dr. Manfred Wendisch und Juniorprof. Dr. Heike Kalesse-Los who acted as the co-reviewers of this PhD thesis.

My sincere thanks to Prof. Dr. Miguel Friz Carrillo of the Universidad del Bío-Bío, Chillán, Chile. Professor, I will be eternally grateful for your words of support and the confidence placed in me.

I would also like to extend my thanks to Holger Schilke, without whom my IMuK stay would have been a great deal harder. Holger, I still remember my arrival in IMuK ... my level of German was quite basic, but I remember long conversations in which you explained to me with all the details how the Institute worked and the measurements. I think I still owe you the invitation to the Christmas market, ups!

I would also like to thank my colleagues and friends who directly or indirectly helped me in the outcome of this thesis. My sincere thanks to the German Academic Exchange Service (DAAD) for financing this investigation.

To my parents, Juana C. González J. and Manuel A. Crisosto O. for their wise advice, for always trusting me, for supporting me in the decisions and challenges that I have proposed so far and their infinite unconditionality. Thank you so much!

To my wife and son...